Petrophysical characterization and thermal conductivity prediction of serpentinized peridotites

Nadjib Chibati, Yves Géraud, Khalid S. Essa

Geophysical Journal International

Geophys. J. Int. (2022) **231,** 1786–1805
Advance Access publication 2022 July 27
GJI Rock and Mineral Physics, Rheology

https://doi.org/10.1093/gji/ggac288

Petrophysical characterization and thermal conductivity prediction of serpentinized peridotites

Nadjib Chibati,[1] Yves Géraud[1] and Khalid S. Essa[1,2]

[1]*Université de Lorraine, UMR 7359 GeoRessources, Ecole Nationale Supérieure de Géologie, 2 Rue du Doyen Marcel Roubault, Vandoeuvre-lès-Nancy* 54000*, France. E-mail: nadjib.chibati@univ-lorraine.fr*
[2]*Faculty of Science, Geophysics Department, Cairo University, Giza* 12613*, Egypt*

Accepted 2022 July 24. Received 2022 June 2; in original form 2021 December 17

SUMMARY

We investigated 22 different serpentinization level peridotite samples from the North Pyrenean Zone (NPZ) and along the North Pyrenean Fault (NPF) to characterize their mineralogical composition and petrophysical properties (bulk and grain density, porosity, compressional and shear wave velocities, and thermal conductivity and diffusivity). Peridotites have a percentage of serpentine that varies between 5 and 97 per cent for fresh samples and totally altered ones, respectively. The mineralogical changes by serpentinization induced a wide variety of petrophysical properties. The key indicators of serpentinization from petrophysical properties in serpentinized peridotite include an increase in porosity of up to 10 per cent and the associated decrease in the solid density ranging from 3.29 g cm^{-1} for fresh peridotites to 2.5 g cm^{-3} for the totally serpentinized peridotites. Thermo-physical properties were found to follow the same deceasing trend as the serpentinization increases up to 3000 m s^{-1} and 1.85 W m^{-1} K^{-1} for *P*-wave velocity and thermal conductivity (TC), respectively. For TC estimation, empirical relationships were produced using multiple linear regression (MLR) and a mineralogy model. For the mineralogy model, we used 10 mixing models commonly used in indirect TC estimation based on mineral composition. For the mean TC of individual mineral phases, the TC estimation shows that in case of non-availability of the proper samples for direct measurement, the TC of peridotite can be inferred with an acceptable level of error from the geometric mean model and harmonic mean models for the dry and saturated conditions, respectively. Based on the results of MLR, the study also confirms that the TC of dry rocks can be predicted through acoustic velocity, density and porosity with a prediction accuracy of $\pm$0.24 W m^{-1} K^{-1} and confidence of $>$80 per cent.

Key words: Permeability and porosity; Heat flow; Acoustic properties; Microstructure.

1 INTRODUCTION

Among the physical properties of materials, thermal conductivity and heat capacity are essential parameters for understanding and modelling different structures from the reservoir scale to the lithosphere scale and passing through the basin scale. Thus, these characteristics are crucial for the study of energy geosystems such as geothermal systems (Deo *et al.* 2014; Förster *et al.* 2015; Omodeo-Salé *et al.* 2020), energy storage (Clauser 2011), heavy oil recuperation (Chekhonin *et al.* 2021) and waste storage or transfer to surface environments (Krzeminska *et al.* 2012). These features are also crucial for the study of continental and oceanic lithosphere structure and transfers (Clauser *et al.* 1997; Mckenzie *et al.* 2005; Hieronymus & Goes 2010), which can condition the distribution of crustal or lithospheric scale structures or the rheology of these structures (Duretz *et al.* 2014).

The physical properties of rocks depend on their mineralogical composition, texture (size, shape and arrangement of mineral grains, nature of grain-to-grain contacts), the degree of alteration of protolith, the characteristics of the pore space (volume, size, shape), the kind of fluid suturing pore space (Clauser & Huenges 2013; Diamantis *et al.* 2014; Albert *et al.* 2017; Garcia & Santamarina 2021) and also on temperature and pressure. Thus, thermal conductivity varies over more than an order of magnitude as a function of these different characteristics (Clauser & Huenges 2013). Significant variability has been measured both at the sample scale (Surma & Geraud 2003; Haffen *et al.* 2017) and at the borehole scale (Pribnow & Sass 1995; Hartmann *et al.* 2005; Mottaghy *et al.* 2005; Haffen *et al.* 2013). This variability is also significant as a function of temperature and pressure (Vosteen & Schellschmidt 2003; Chang *et al.* 2017; Chekhonin *et al.* 2021) and as the H_2O contents of the mineral phases (Chang *et al.* 2017; Zhang *et al.* 2019). Nevertheless,

these characteristics remain rather poorly documented compared to other physical properties.

The study of crustal and lithospheric structure based on macroscopic data, such as *P*-wave (V_P) and *S*-waves (V_P) velocities and heat flow. TC is thus a crucial parameter if we wish to reconstruct these structures or identify heterogeneities, but TC values are very often average values that take little account of heterogeneities (Hieronymus & Goes 2010). Thus, several works have attempted to define relations between the different petrographic and petrophysical characteristics and the thermal properties of different types of materials (Yaşar *et al.* 2008; Jorand *et al.* 2013; Pimienta *et al.* 2014; Esteban *et al.* 2015; Rachel Jorand *et al.* 2015; Gu *et al.* 2017; Mielke *et al.* 2017).

Peridotite is the most important rock type of both continental and oceanic lithospheres. These rocks can be altered to serpentine through hydration by seawater or hydrothermal water. These serpentinite are quite frequently described in tectonically active zones such as oceanic ridges (Falcon-Suarez *et al.* 2017), subduction zones (Ohtani 2020), mountain chains with ophiolite series (Katayama *et al.* 2020) and more locally in crustal or lithospheric fault zones like the San Andreas Fault (Moore *et al.* 2016) and in fracture zones associated with transform faults of slow ridges and oceanic hydrothermal systems(Grevemeyer *et al.* 1999). In these different geological contexts, peridotites are subject to mineralogical, textural, and mechanical properties variations. These variations lead to the wide variability of physical properties measured under the surface and underground conditions (Christensen 1966; Gibert 2003; Xu *et al.* 2004; Jacobsen *et al.* 2008; Dobson *et al.* 2010; Chang *et al.* 2017). These petrographic facies and the associated properties change have consequences for fault rheology (Christensen 2004; Moore *et al.* 2016).

Only a few studies have reported a complete view of the petrophysical properties of peridotites and the effect of the serpentinization on these properties (Gibert 2003; Bach *et al.* 2004; Christensen 2004; Schmitt *et al.* 2007; Diamantis *et al.* 2009, 2011, 2014; Ge *et al.* 2021; etc.). However, to date there has been no combined approach that compares a range of quantified serpentinization intensity to petrophysical properties. In the present study, we focused on the characterization of petrophysical and mineralogical evolution of the North Pyrenean fractured and serpentinized peridotite, and we introduce a framework to evaluate petrophysical property variations corresponding to serpentinization intensity. The properties of the rocks were characterized by microscopic analysis of thin sections and petrophysical measurements [porosity, density, TC, thermal diffusivity (TD) and *P*-and *S*-wave propagation velocities under dry and saturated conditions (V_{Pd}, V_{Sd}, V_{Ps}, V_{Ss}, respectively)]. These properties are suitable for the interpretation of will-log data and reservoir modelling. The link between these properties will be discussed through analysis of the relation between thermal conductivity and the other measured petrophysical properties to propose empirical relationships to the indirect prediction of TC. Two approaches were used for the indirect prediction of TC: (I) numerical mixing models deploying the mineralogical composition, porosity and composition of saturation fluids (Clauser 2011) and (II) correlation of thermal conductivity with other physical properties (Gąsior & Przelaskowska 2014; Fuchs *et al.* 2015, 2018).

2 GEOLOGICAL SETTING AND SAMPLING

The Pyrenees is a narrow 400 km long and 100 km large mountain chain oriented N 110° between the Iberian plate and the Eurasian plate, created by the north–south convergence and the partial continental subduction of the Iberian plate under the Eurasian plate from the Upper Cretaceous to the Lower Eocene (Choukroune 1989; Beaumont *et al.* 2000; Mouthereau *et al.* 2014). The Pyrenean orogeny results from the closure of intercontinental basins between Iberia and Europe, formed during the Mesozoic extension (Jammes *et al.* 2009; Lagabrielle *et al.* 2010). The bottom of these basins is composed of hyper-thinned continental crust and locally of an outcropping subcontinental mantle(Lagabrielle & Bodinier 2008; Jammes *et al.* 2009). Typically, the Pyrenean orogeny is subdivided into five tectono-stratigraphic zones (Fig. 1), parallel to the elongation of the Pyrenean chain (Choukroune 1992; Beaumont *et al.* 2000; Ford *et al.* 2016). From north to south, we find the Aquitaine Basin (AB), the North Pyrenean Zone (NPZ), the Axial Zone (AZ), the South Pyrenean Zone (SPZ) and the Ebro Basin (EB).

The NPZ is well-known for the occurrence of about 40 outcrops of subcontinental peridotite lenses ranging from few meters to 3 km in length and widespread in the Mesozoic sediments or the granolithic massifs, parallel to the NPF (Fabriès *et al.* 1998; Lagabrielle *et al.* 2010). Since 1980, the Pyrenean peridotites had been interpreted as hot solid intrusive bodies in the upper crust causing brecciation by decarbonization of limestone and dolomite and liberation of CO_2 gas (Minnigh *et al.* 1980). Vielzeuf & Kornprobst (1984) suggested that these peridotites lenses were mantellic intrusions into a thinned crust during the Albian extension and subsequently incorporated into the chain during Tertiary compression. The discovery of exhumed lithospheric mantle at the base of some non-volcanic passive margins (Boillot *et al.* 1987) led to new models being proposed that suggest that the mantle exhumation occurred in the context of distal passive margin (Lagabrielle & Bodinier 2008; Jammes *et al.* 2009). The Cretaceous extension and the opening of the Bay of Biscay caused extreme crustal thinning and the exhumation of the upper mantle at the bottom of the Albian basins along the NPF. Due to the high thermicity, the distal part of this margin was deformed in a ductile manner without typical fragile structures of passive margins (Clerc *et al.* 2012).

The rock samples studied in this paper were collected from the peridotite lenses situated in the NPZ and along the North Pyrenean Fault (NPF). Their localization is given in Fig. 1 (white circles).

3 MATERIEL AND METHODS

3.1 Petrographic study

Our description of the petrographic composition of the peridotite samples was based on the study of 25 representative thin sections using a polarized microscope. These thin sections were produced from the same samples on which the petrophysical measurements were performed. The aims of the microscopic study of these thin sections ware to identify the primary and secondary mineral phases, differentiate the types of pore spaces and estimate the density of microfractures. Also, the volume fraction of serpentine for each sample was calculated using measured densities values and is described in part 3.5.

3.2 Porosity and density measurements

Porosity is defined as the proportion of the vacuum existing in rock and expressed as the ratio between the voids' volume and the total volume of the rock sample (Bourbié *et al.* 1986). The quantification of the porosity is fundamental to assess the storage capacity of the

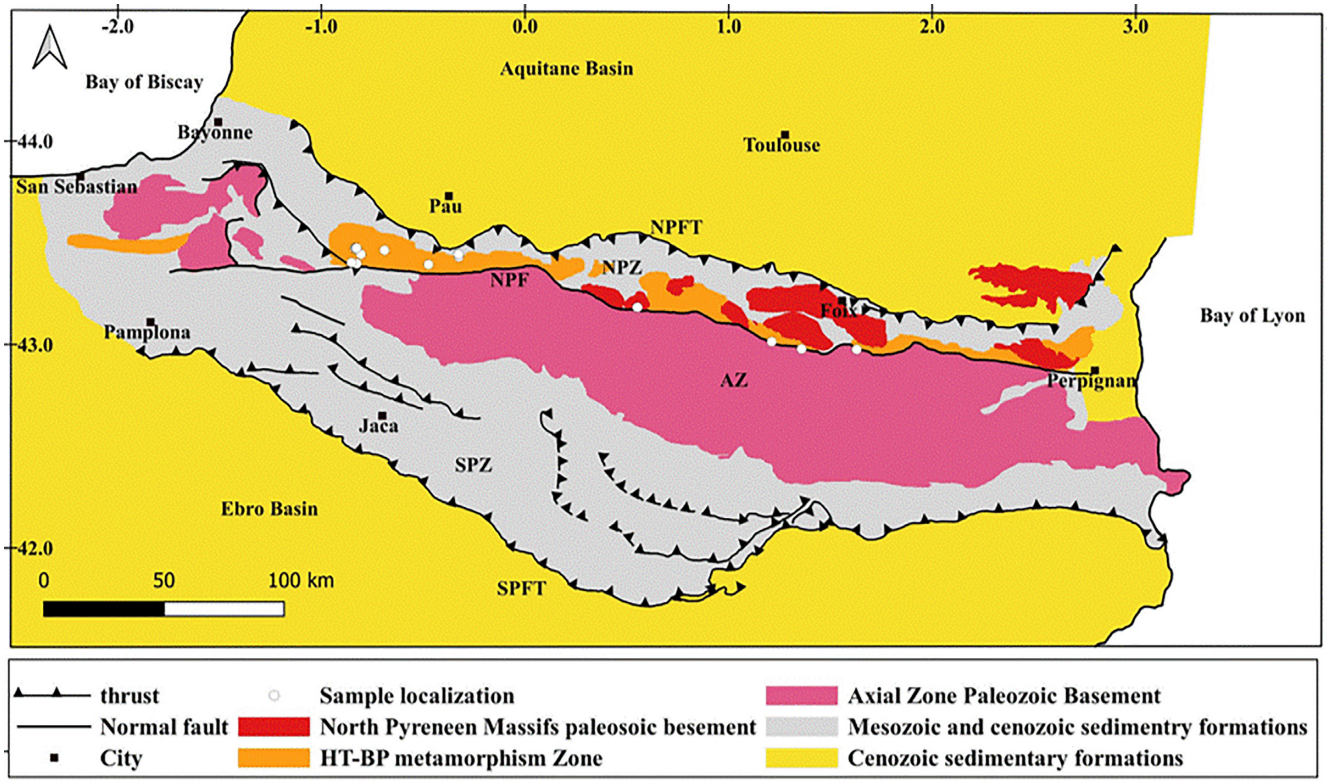

Figure 1. Simplified geological map of the Pyrenees chain. Adapted from Ford *et al.* (2016) and Clerc *et al.* (2012). With the localization of the samples used in this study (white circles). Abbreviations: AB, Aquitaine Basin; NPZ, North Pyrenean Zone; AZ, Axial Zone; SPZ, South Pyrenean Zone; EB, Ebro Basin; NPFT, North Pyrenean Frontal Thrust; SPFT, South Pyrenean Frontal Thrust, NPF, North Pyrenean Fault.

rocks and reservoirs. Pore volume, pore morphology and the quality of pores connection are also critical because they influence other petrophysical properties.

The triple weighting method is well defined by the RILEM norm (try n°I.1. 1978). This is a consistent low-cost and easy method which permits measurement of the porosity (φ), bulk (ρ_b) and grain (ρ_s) densities. After drying samples in the oven at 60 °C until their mass (M_{dry}) was stable, the rock samples were placed in the desiccator for 1 h to eliminate the gas from the pores. Then, samples were saturated with water beneath a vacuum for at least 24 hr before the weight of the saturated samples (M_{sat}) and their hydrostatic weight (M_{hyd}) were measured. Thus, porosity (φ), bulk density (ρ_b) and grain density (ρ_s) can be expressed by the following eqs 1–3, respectively,

$$\varphi = \frac{M_{sat} - M_{sec}}{M_{sat} - M_{hyd}} \times 100, \quad (1)$$

$$\rho_b = \frac{M_{sec}}{M_{sat} - M_{hyd}}, \quad (2)$$

$$\rho_s = \frac{M_{sec}}{M_{sec} - M_{hyd}}. \quad (3)$$

3.3 Thermal conductivity and thermal diffusivity measurements

In this study, the thermal conductivity scanner (TCS) was used to measure the TC and TD of the rock samples under ambient conditions. TCS is a contactless optical scanning method derived by Popov *et al.* (1999). The measuring instrument has a mobile plate composed of a heat source and three thermal sensors for measuring temperature variation before and after sample heating. The measurement procedure has been described by Popov *et al.* (1999, 2016) and Boulanouar *et al.* (2013). For the measurements, the rock samples were cut into parallelepipeds and then painted black to homogenize the reflection coefficient. Under dry and water-saturated conditions, the TC and TD were measured in the three directions of parallelepiped blocks and then the average of the TC and TC in each direction was calculated to assess the possible anisotropy due to the alteration, fractures and mineral foliation.

3.4 Elastic wave velocities measurements

The compressional wave velocity (V_P) and shear wave velocity (V_S) through samples were carried out on the dry and saturated samples under atmospheric conditions, using a commercial ultrasound generator (Proceeq^R brand Pundit lab model) (Navelot *et al.* 2018). The instrument is composed of a pulse generator and two piezoelectric transducers of 54 and 250 kHz for V_p and V_s acquisitions, respectively. For each measurement, the emitter and receiver are pressed against two parallel faces of a parallelepiped sample. A contact gel was applied to ensure a better wave transmission and limiting surface effects. Then, a continuous measurement was performed using the adequate frequency. V_p and V_s were measured on both dry and water-saturated rock samples as well as along three directions that were oriented perpendicular to each other to estimate the anisotropy linked to the alteration, fractures and mineral foliation.

3.5 Thermal conductivity modelling

TC is crucial for evaluating heat flow that is an indispensable parameter in any thermal modelling. TC data are essential when studying the thermal evolution of crystalline areas and sedimentary basins and important for geothermal energy exploration, heat and gas storage (Abdulagatova *et al.* 2009; Clauser 2011; Haffen *et al.* 2013).

Thermal conductivity is difficult to measure directly in the field or borehole and so indirect methods can be used to overcome such situations. Two indirect methods are frequently used to estimate thermal conductivity: (I) TC is assessed from the mineralogical composition of the rock and porosity applying TC of each mineral and TC of saturation fluids by using the mathematical mixing models presented below. (II) TC can be related to the more easily measured physical properties in the borehole, for example through the application of MLR analysis. For this method a calibration based on laboratory data is necessary.

The first approach is essentially performed in the case of low porous igneous and metamorphic rocks (Horai & Baldridge 1972; Pribnow & Umsonst 1993; Pribnow & Sass 1995; Clauser 2011; Ray *et al.* 2015; Zhao *et al.* 2016; Chopra *et al.* 2018; Fuchs *et al.* 2018, 2021) and to determine the bulk TC of sedimentary rocks assuming the solid matrix and the pore space are the two components of the rock's system (Fuchs *et al.* 2013; Albert *et al.* 2017). This method presents some limitations and uncertainties due to the need for both precise mineralogy of the rocks and the TCs of each mineral phase.

The following two important assumptions were made for peridotite TC modelling from this first approach:

(i) Olivine and serpentine are the main solid phases that contribute to the TC of the peridotite. The applicability of the models is limited to the case where the bias introduced by the secondary minerals is very low. The protolith must be an olivine-rich peridotite and/or the mean TC of olivine and pyroxene should be very close (Table 2).

(ii) The volume fraction (Serp°) of serpentine in each sample was determined using relation (Serp° $= (\rho_{ol\_} \rho_s)/(\rho_{ol} - \rho_{serp})$ $= (3.33 - \rho_s)/0.785$) (Karson *et al.* 1997; Miller & Christensen 1997), where ρ_s is the solid density of the samples measured by weighting method and $\rho_{ol} = 3.3$ g cm^{-3} and $\rho_{serp} = 2.515$ g cm^{-3} are the mean densities of olivine and serpentine. The volume fraction of olivine equals (1 − Serp°). Then, the individual mean mineral TC, the TC fluid saturating pores (λ_i; Table 2), and the volume fraction (X_i) of the *i*th phase relative to the total volume (considering porosity) were used to calculate the TC (λ_{cal}) using the mixing models (eqs A1–A9; see the Appendix). The physical background of these models is extensively detailed in Hartmann *et al.* (2005), Clauser (2009), Ray *et al.* (2015) and Jia *et al.* (2019).

The second approach aims to find empirical correlations between thermal conductivity and other petrophysical properties measured in the laboratory and boreholes (Özkahraman *et al.* 2004; Hartmann *et al.* 2005; Goutorbe *et al.* 2006; Fuchs & Förster 2010, 2014; Gegenhuber & Schoen 2012; Gąsior & Przelaskowska 2014; Mielke *et al.* 2017). This kind of approach enables the prediction of TC from single or several petrophysical properties of the rocks using statistical regression methods. However, until now no universal TC prediction equations have been developed. The empirical equations based on these regression methods are typically limited to the rocks (types, lithology, chemical composition, etc.) for which they were established.

4 RESULTS

4.1 Petrography

The petrographic study of Pyrenean peridotite led us to define three main levels of serpentinization. As had already described in the literature by Fabriès *et al.* (1998), the fresh to low altered samples (Figs 2a–c) have a classic composition of spinel lherzolite, with the subhedral porphyroclastic forms of mineral and grain size of 0.1–4 mm. The low-grade alteration samples are composed mainly of olivine (>80 per cent) and pyroxene (from 5 to 10 per cent) as major mineral phases and accessory mineral phases (spinel and opaque minerals). At the thin section scale, serpentine and opaque minerals appear as small black veinlets, localized mainly in the borders of minerals and rarely in the microfracture of olivine grains (PY17_1 and PY17_10; Fig. 2a). Pyroxenes are generally not altered. Spinels are often dark green and present a cracked texture. A small micrometric halo of magnetite crystallizes in the microfracture network and around borders of spinel grains. The porosity is composed of microfractures. Their increases as the sample's alteration increases.

Moderately to highly altered samples (PY17_5, PY17_12, PY17_13) are characterized by a high and moderate transformation of olivine and pyroxenes, respectively (Figs 2e and f). The observations of thin sections revealed that the serpentine crystallizes in a centripetal manner around the olivine grains, leading to a pseudomorphic-mesh texture with a core of relict olivine (Fig. 2e). The relicts of olivine were transformed to serpentine in some samples, but the shape of these olivine grains was still visible (Fig. 2f). Pyroxenes were found to have a less pronounced alteration, except for some orthopyroxene crystals which lost their optical characteristics (Fig. 2d). The serpentine in the pyroxene crystals was found to occur in fan-shaped aggregates distributed along the two cleavage planes and around the grains. The spinel minerals are usually dark green to opaque and have a cracked texture and are also slightly transformed into magnetite minerals. In some thin sections (PY17_12), the second generation of serpentine associated with magnetite crystallizes in the fractures, which lead to the reduction of porosity (Fig. 2d).

Moderately to highly altered samples show a visible increase in microfracture densities. The porosity is composed of some micropores formed during the alteration of the primary minerals and microfractures which are not filled by serpentine and magnetite minerals (Fig. 2f).

Totally altered samples (Figs 2g–i) are characterized by large serpentine development. Olivine, pyroxene and spinel were fully transformed to massive serpentine and magnetite minerals, whereas ghosts of pyroxene were still visible in some thin sections (Fig. 2i). Magnetite minerals were also present in the fractures. In the totally altered samples, three generations of serpentine were observed (Fig. 2h) as follows; massive serpentine from the replacement of minerals of olivine and pyroxene and two other generations of serpentine which crystallized in the fractures (Figs 2g and h). These samples are characterized by a massive increase of micro- and macrofractures densities. These fractures may be unfilled and form fracture porosity. In some thin sections, these fractures were found to be filled by the two late generations of serpentine and associated magnetite .

4.2 Petrophysical properties

4.2.1 Porosity and densities (bulk and grain)

The grain (ρ_s) and bulk (ρ_b) densities of the peridotite samples were measured using the water saturation method and the results

Table 1. List of measured petrophysical properties and localization of the 22 studied lherzolitic peridotite samples: grain density (ρ_s), bulk density (ρ_b), porosity (φ), degree of serpentinization (serp°), dry thermal conductivity (λ_d), saturated thermal conductivity (λ_s), dry thermal diffusivity (D_d), saturated thermal diffusivity (D_s), dry *P*-wave velocity (V_{Pd}), saturated *P*-wave velocity (V_{Sd}), dry *S*-wave velocity (V_{Sd}), saturated *S*-wave velocity (V_{Ss}), Young's modulus (E) and Poisson's ratio (υ).

Sample no	Latitude	Longitude	Alteration state	ρ_s (g cm^{-3})	ρ_b (g cm^{-3})	φ (%)	Serp° (%)	λ_d (W m^{-1} K^{-1})	λ_s (W m^{-1} K^{-1})	D_d (mm^2 s^{-1})	D_s (mm^2 s^{-1})	V_{Pd} (m s^{-1})	V_{Ps} (m s^{-1})	V_{Sd} (m s^{-1})	V_{Ss} (m s^{-1})	E (GPa)	υ
PY17_1	42.80662	1.37294	Fresh to slightly altered	3.26	3.21	1.55	9.2	3.72	4.05	1.63	1.68	5161	6734	2790	2977	64.60	0.29
PY17_5	42.97545	0.71085	Fresh to slightly altered	3.24	3.07	5.34	11.2	3.13	3.75	1.30		4078	5623	2206	2806	39.00	0.29
PY17_7	42.97586	0.7145	Fresh to slightly altered	3.01	2.88	4.54	40.5	2.53	2.72	1.30	1.48	4398	5592	2179	2272	36.51	0.34
PY17_10	42.77091	1.51988	Fresh to slightly altered	3.29	3.25	1.18	5.4	4.23	4.28	1.76	1.86	7206	7300	3693	3378	117.18	0.32
PY17_3	43.06734	−0.31308	Moderately altered	3.21	3.14	2.21	15.5	3.51	3.73	1.60	1.56	6247	6650	3219	2947	85.77	0.32
PY17_13	43.1165	−0.6746	Highly altered	2.76	2.56	7.36	72.2	1.93	2.09	0.89	1.03	4908	5466	2404	2410	39.71	0.34
PY17_24	42.76848	1.79069	Totally altered	2.69	2.54	5.88	81.1	1.85	2.03	0.81	1.08	4471	5040	2295	2145	35.28	0.32
PY17_36	43.13734	−0.16494	Totally altered	2.64	2.55	3.34	87.6	2.77	2.93	1.06	1.46	5084	5282	2488	2413	42.43	0.34
PY17_57	43.1181	−0.66624	Highly altered	2.73	2.47	9.72	75.9	2.22	2.24	1.01	1.19	4590	4926	2574	2789	43.24	0.27
PY17_55	43.11714	−0.6686	Totally altered	2.64	2.44	7.45	88.3	2.11	2.24	1.16	1.18	4407	4815	1926	2659	25.02	0.38
PY17_44	43.0026	−0.65314	Highly altered	2.74	2.55	6.90	75.7	2.76	2.96	1.51	1.48	4897	5699	2880	2502	52.23	0.24
PY16_1	43.13769	−0.1663	Moderately altered	2.80	2.69	4.06	67.5	2.72	2.68	1.11	1.68	5918	6000	3867	3003	90.57	0.13
PY17_14	43.11803	−0.6695	Totally altered	2.66	2.39	9.93	85.0	2.20	2.39	0.96	1.05	3486	6343	1872	3028	21.76	0.30
PY17_20	43.06128	−0.66502	Totally altered	2.67	2.52	5.44	84.5	2.69	2.87	1.02	1.26	3677	4723	2013	2622	26.28	0.29
PY17_21	43.06127	−0.66502	Totally altered	2.67	2.39	10.45	83.8	1.97	2.27	0.66	1.06	3451	4452	1790	2348	20.18	0.32
PY17_31	43.13781	−0.16448	Totally altered	2.66	2.42	9.00	85.5	2.12	2.28	0.99	1.20	3671	4547	2037	2492	25.66	0.28
PY17_17	43.11721	−0.66977	Totally altered	2.69	2.48	7.68	82.0	2.59	2.87	1.10	1.45	3928	4698	2425	2213	34.76	0.19
PY17_48	43.06127	−0.6652	Totally altered	2.69	2.44	9.45	81.0	2.49	3.00	1.20		3312	4392	1820	2339	20.74	0.28
PY17_35	43.13708	−0.16763	Totally altered	2.57	2.43	5.45	97.1	1.99	2.11	0.80	1.25	4608	4711	2291	2277	34.05	0.34
PY17_30	43.13781	−0.16448	Highly altered	2.75	2.73	0.91	73.8	2.93	2.99	1.15	1.49	5627	5627	2807	3003	57.32	0.33
PY17_58	43.06335	−0.49144	Highly altered	2.716	2.43	10.1	78.2	1.99	–	0.73	–	4608	–	–	–	–	–
PY17_12	43.11654	−0.67455	Moderately altered	2.85	2.83	0.91	60.6	2.75	2.77	1.10	1.15	6099	6343	3020	3028	69.00	0.34

Table 2. Compilation of the average TC of the major minerals' phases present in the studied rocks; (1) Birch & Clark (1940); (2) Kanamori *et al.* (1968); (3) Beck *et al.* (1978); (4) Horai &Simmons (1969); (5) Horai (1971); (6) Horai & Baldridge (1972); (7) Clauser & Huenges (2013); (8) Schön (2011).

Mineral	λ (W m^{-1} K^{-1})			Number of data	Sources
	Min	Mean	Max		
Olivine	3.91	4.78	5.16	14	1,2, 4, 6, 7, 8 6
Serpentine	2.14	2.77	3.7	8	1, 2, 6, 7,8
Pyroxene	3.82	4.61	5.57	16	1,2, 4, 6, 7, 8 6
Spinel	9.48	11.8	14.44	5	1, 3, 6, 7, 8
Water	–	0.6	–	–	8, 6
Air	–	0.026	–	–	7, 6

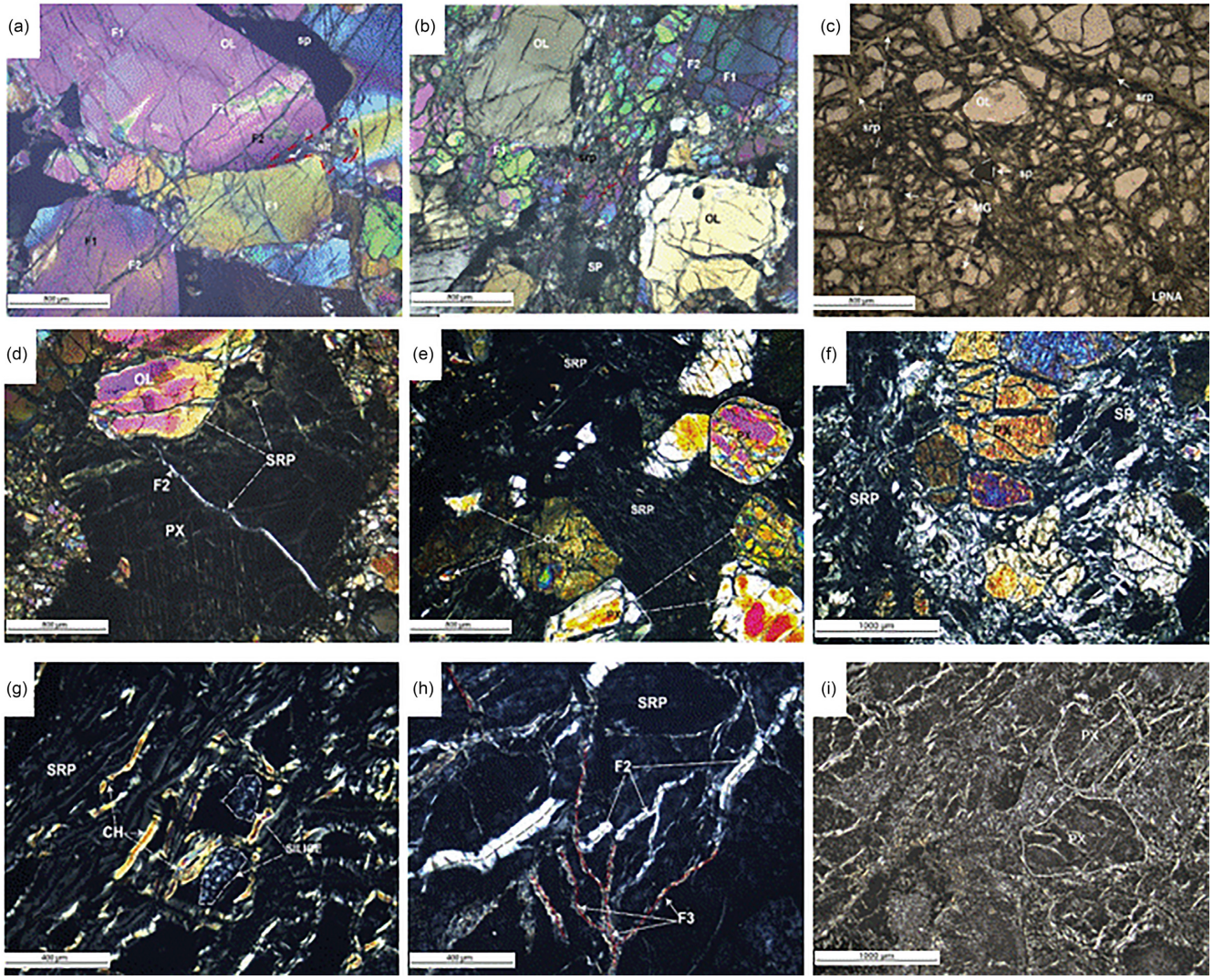

Figure 2. Thin sections photomicrographs of different grad altered peridotite: (a–c) Low grad altered samples; (d–f) moderately highly altered samples; (g–i) totally altered samples. Abbreviation: OL, olivine, PX, pyroxene, SP, spinel, SRP, serpentine, CH, chrysotile, F1, intracrystalline fracture; F2 and F3, second and third generations of fractures, respectively.

are presented in Fig. 3 and Table 1. The grain density of the peridotite samples varies widely between 2.56 and 3.29 g cm^{-3}, with an average of 2.80 g cm^{-3} (Table 1). This variation reflects the change in the mineralogical composition of the fresh and altered samples. This change in density is directly correlated with the serpentine content. Indeed, there is a systematic decrease of solid density as the serpentinization increases (Fig. 3c). During serpentinization, olivine and pyroxene minerals with mean densities of 3.33 and 3.36 gcm^{-3} respectively, were progressively transformed to serpentine with an average density of 2.6 g cm^{-3} (Schön 2011). The value of grain density was used to define the degree of serpentinization.

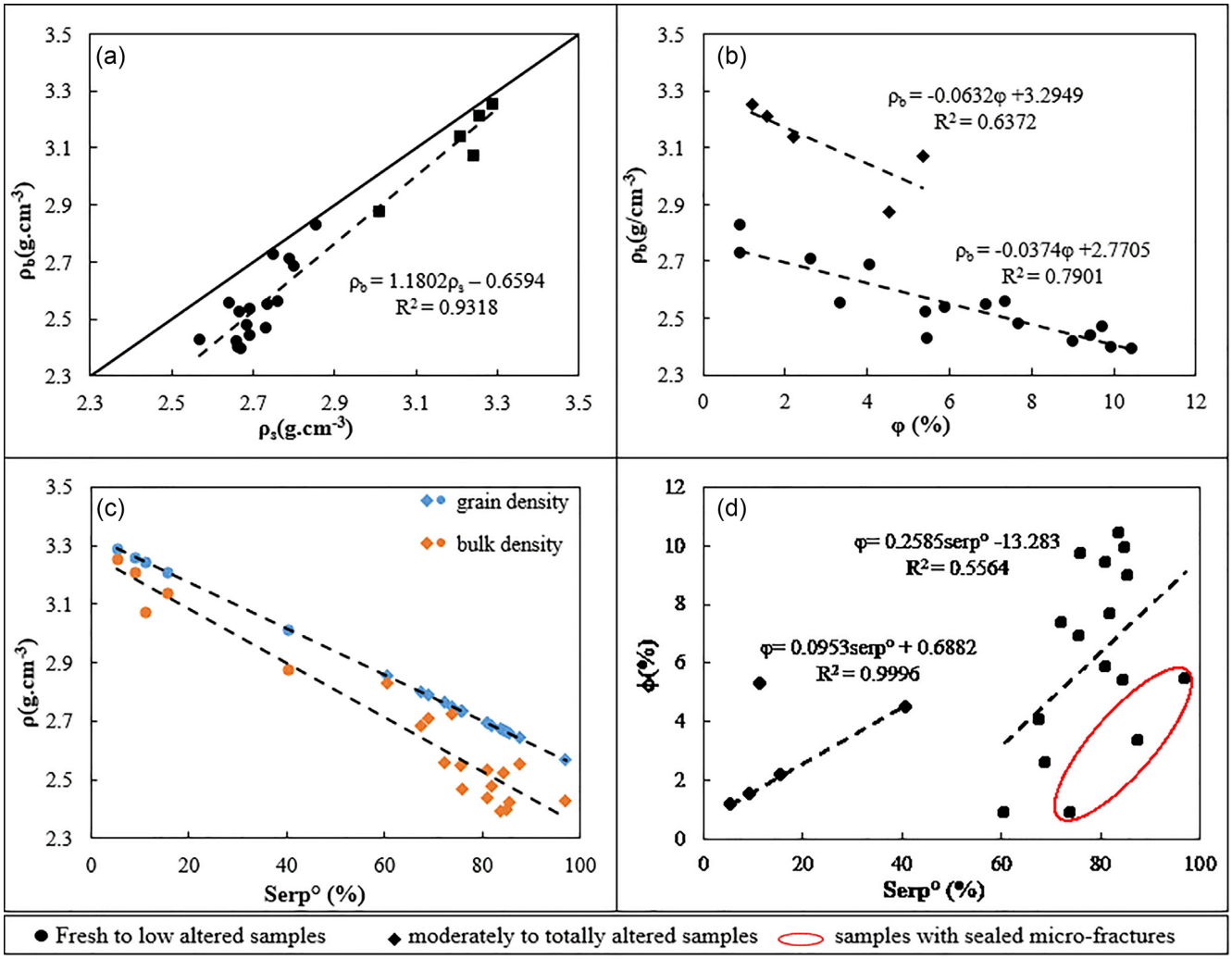

Figure 3. Petrophysical properties of the investigated peridotites: (a) Grain density versus bulk density; (b) bulk density versus water porosity; (c) grain and bulk densities versus degree of serpentinization; (d) porosity versus degree of serpentinization.

The bulk density (ρ_b) ranged from 2.39 to 3.21 g cm^{-3} with a mean value of 2.65 g cm^{-3}, and very low porous samples were found to have a bulk density closer to the grain density. The bulk density shows a positive linear relationship with grain density (Fig. 3a) and a negative relation with porosity (Fig. 3b). Indeed, as seen in numerous studies (Boulanouar *et al.* 2013; Navelot *et al.* 2018; Bertrand *et al.* 2021), the bulk density is a function of grain density and porosity. The plot of bulk density vs. degree of serpentinization displays a negative linear relationship ($\rho_b = -0.0093\text{Serp}^\circ + 3.2695$) with a good correlation factor ($R^2 = 0.94$). This relationship can be explained by the fact that the alteration decreases the bulk density through replacing dense minerals (olivine and pyroxene) with low-density minerals (serpentine).

The porosity of the studied samples varies from 0.91 to 10.45 per cent with an average of 5.63 per cent. Porosity variation is controlled by the alteration state, the density of microfractures and the sealing state of the fractures. As Figs 3(b) and (d) show, two groups of samples can be clearly distinguished from the plots of the porosity versus bulk density and porosity versus the degree of serpentinization: (i) the fresh to low altered samples and (ii) moderately to totally altered samples.

For the first group (black square in Figs 3b and d), the porosity ranges from 1.18 to 4.54 per cent with an average value of 2.96 per cent, bulk density is between 2.88 and 3.25 g cm^{-3} and degree of serpentinization is less than 40 per cent, except the PY17_5 sample (φ = 5.34 per cent), which is slightly altered but has a high density of microcracks. With the increase in porosity, the bulk density decreases and the degree of serpentinization increases.

For the second group (black circle in Figs 3b and d), the porosity varies from 3.3 to 10.4 per cent with an average value of 6.3 per cent, degrees of alteration varies between 60 and 100 per cent and bulk density varies between 2.39 and 2.82 g cm^{-3}. This high porosity and high degree of alteration tend to decrease the bulk density compared to those of the first group. Thus, the decrease in the bulk density was found to be controlled by the development of the porosity which is formed by crack and alteration of primary mineral phases. Samples PY17_30, PY17_36 and PY17_12 (circled in Fig. 3d) exhibit low porosity values compared to their alteration state which are due to the sealing of microfracture by the second-generation serpentine described in Section 4.1.

These two groups were defined by the grain density of the main phases and highlighted by the y-intercept corresponding approximately to olivine and serpentine mean densities, respectively (Fig. 3b).

4.3 Thermal and physical properties

The thermal and other physical properties measured on 22 peridotite samples under dry and saturated conditions are summarized in Table 1.

4.3.1 Thermal conductivity and thermal diffusivity

At least three TC and TD profiles were acquired on each face of each parallelepiped. The mean values of TC and TD were calculated for each sample and given in Table 1.

TC depends on mineral composition and the type and the amount of porosity (Clauser 2009). The experiment results of the present study show that the measured TC and TD under dry condition range from 1.86 to 4.23 W m^{-1} K^{-1} with an average value of 2.62 W m^{-1} K^{-1} while TD varies between 0.79 and 1.58 mm^2 s^{-1}, for an average value of 1.14 mm^2 s^{-1}, respectively. A very low value of TC was observed for a totally altered and highly fractured sample (PY17_14) and the highest value was measured from low altered sample (PY17_1). According to the petrographic observations, the comparison between the TC of fresh and altered samples showed a systemic decrease of TC with increasing of serpentinization degree. As the alteration increases, the primary minerals (olivine) with a mean TC of 4.78 W m^{-1} K^{-1} are replaced by the serpentine of mean TC of 2.77 W m^{-1} K^{-1}. The measurements performed in three directions show an anisotropy ranging from 0 to 9 per cent, indicating that the studied rocks are generally isotropic or with a low anisotropy in nature.

The effect of the porosity increases on the CT variation is described in Fig. 4(a) with a logarithmic relationship ($\lambda_d = -0.589 \ln(\varphi) + 3.478$). The phase transformation induced by the serpentinization also influences the TC variation. This phenomenon explains the low correlation coefficient between porosity and dry TC. This joint effect could be described using the correlation between CT and the bulk density. Fig. 4(b) shows a recognizable increase of the TC as the bulk density increases. This relationship can be broken down into three groups of samples with their own equations.

The first group consists of fresh to low altered samples (red circle), they have a bulk density greater than 2.85 g cm^{-3} and a thermal conductivity between 3.13 and 4.23 W m^{-1} K^{-1} with an average of 3.25 W $m^{-1}K^{-1}$ except for samples PY17_3 which have a TC of 2.5 Wm^{-1} K^{-1} due to its high porosity and advanced degree of alteration. The second group is composed of the moderately to highly altered samples (green circle), they have a bulk density between 2.56 and 2.82 g cm^{-3} and their thermal conductivity ranges between 1.75 and 2.91 W m^{-1} K^{-1} (average value is 2.35 W m^{-1} K^{-1}). The third group (purple circle) is composed almost of totally altered samples (degrees of serpentinization > 81 per cent) and have a grain density between 2.39 and 2.5 g cm^{-3} and a thermal conductivity between 1.8 and 2.72 W m^{-1} K^{-1} (with an average of 2 34 W.m^{-1}.K^{-1}). The two last groups had the same average TC, although the density of totally altered samples was lower than those of moderately altered ones. This can be explained by the fact that the serpentine is the main mineral involved in the TC of these samples.

The TC is also measured form the water-saturated samples (Table 1). The TC of the water-saturated samples ranges from 2.02 and 4.28 W m^{-1} K^{-1} for an average of 2.81 W m^{-1} K^{-1}. The TC of wet samples is always greater than the TC of dry samples and the difference between both increases as the porosity increase. This evolution reflects the considerable difference between the TC of water (0.6 W m^{-1} K^{-1}) and air (0.026 W m^{-1} K^{-1}).

TD is a function of TC, density and heat capacity. The TD of the samples falls between 0.66 and 1.76 mm^2 s^{-1} with an average of 1.15 mm^2 s^{-1} in dry condition and between 1.03 and 1.85 mm^2 s^{-1} for an average of 1.34 mm^2 s^{-1} in water-saturated conditions. Fig. 4(c) shows a relatively good correlation between TC and TD ($D = 0.4075\lambda + 0.0698$ with $R^2 = 0.757$) as in the case of TC.

4.3.2 P-wave velocity (V_P) and S-wave velocity (V_S)

The measurements of V_P and V_S were performed on dry and water-saturated conditions (V_{Pd}, V_{Sd} and V_{Pd}, V_{Ss}, respectively) and are shown in Table 1 and Fig. 5. The V_{Pd} falls between 3321 and 7260 m s^{-1} with an average of 4592 m s^{-1}. The highest values of V_{Pd} were obtained from non-fractured samples and low serpentinization level and the lowest values are found in highly serpentinized samples. Indeed, the graphic representation of V_{Pd} versus bulk density (Fig. 5a) highlights three groups.

(i) The fresh to low altered samples (red circle) display high density (> 2.87 g cm^{-3}) and a high compressional wave propagation velocity (ranging from 7200 to 4400 m s^{-1}) with an average value of 5418 m s^{-1}. However, the development of the fracture network in some samples (eg. PY17_5, PY17_1) creates discontinuity surfaces, this in turn decreases the velocities of the samples close to those of the highly altered samples and increases their anisotropy up to 20 per cent. For these samples, the lower V_{Pd} values were recorded perpendicularly to the dominant fracturing direction inferred from the oriented thin section.

(ii) The second group is composed of totally altered and highly fractured samples (purple circle). These samples are composed of serpentine and have an average density value of 2.44 g cm^{-3}. The V_{Pd} of these samples is ranging between 3000 and 4600 m s^{-1}, with an average value of 3881 m s^{-1}. The low V_{Pd} values are due to the high density of microfractures, the small size of the alteration mineral and the characteristic of serpentine (5000 m s^{-1}; Schön 2011). The V_{Pd} anisotropy for the samples was found to range between 1 per cent and 15 per cent (average value is 7.8 per cent) and was higher than the TC anisotropy which has a mean of 1 per cent for this group. This more marked V_{Pd} anisotropy can be attributed to the microfracture shape and orientation.

(iii) The third group is composed of moderately to highly altered samples (green circle). The samples have an average bulk density of 2.66 g cm^{-3} and their V_{Pd} ranging between 4300 and 6330 m s^{-1} with an average of 5113 m s^{-1}. These samples constitute an intermediate group between the both previous groups with a degree of serpentinization between 64 and 81 per cent. The uniform distribution of alteration minerals and fractures filled by the secondary serpentine were found to lead to the lowest anisotropy in the V_{pd} measurement, indicating that these samples are isotropic.

The compressional wave velocity shows an inverse correlation with porosity (Fig. 5b; $V_{pd} = -1060 \ln(\varphi) + 6263.1$). As the results show, the correlation coefficient between the porosity and V_{Pd} is low ($R^2 = 0.6309$). This demonstrates that the decrease in V_p is partially due to mineralogical transformations during alteration and not just to the increase in porosity.

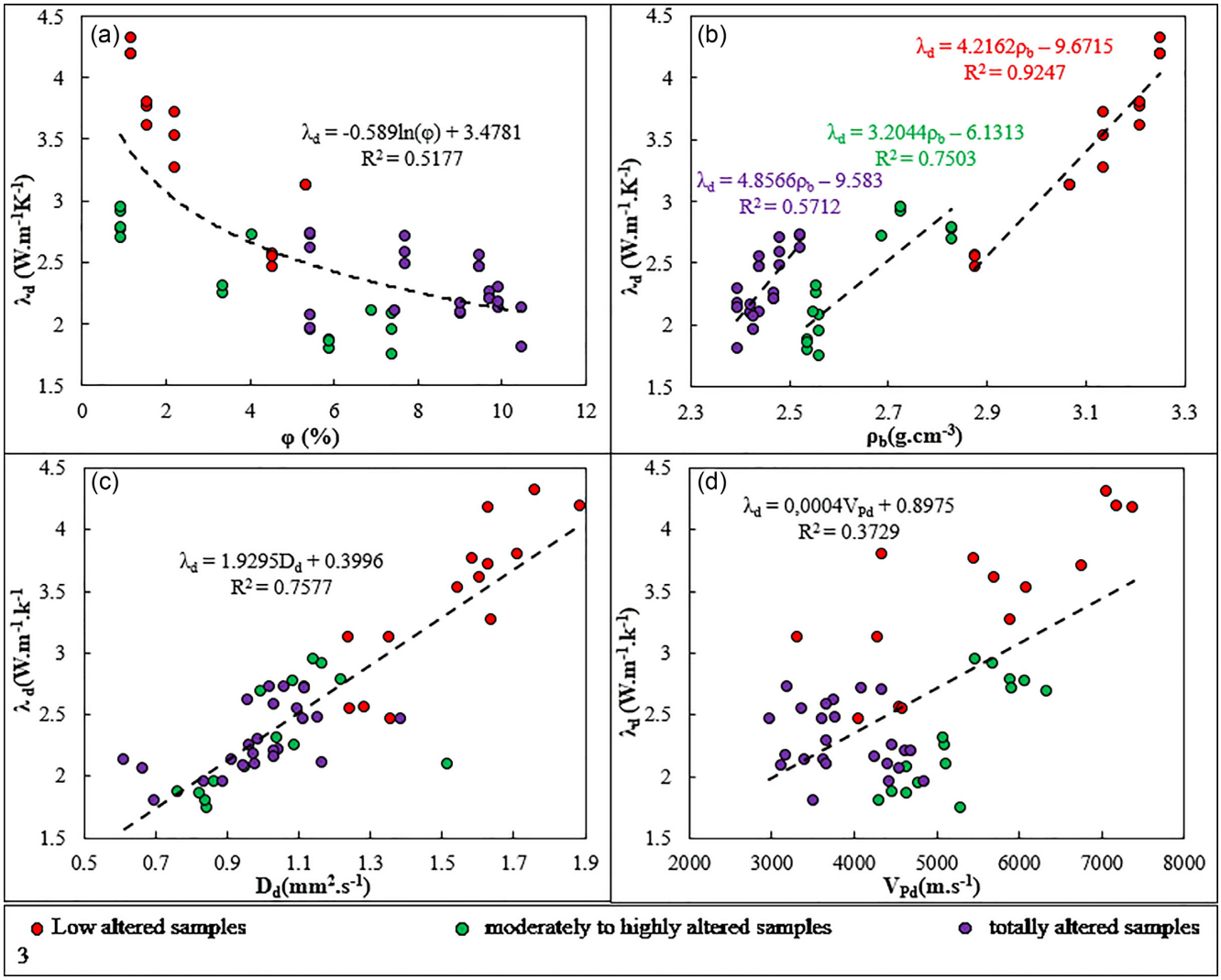

Figure 4. Thermal properties of the investigated peridotite: (a) TC versus porosity; (b) TC versus bulk density; (c) TD versus thermal conductivity; (d) TC versus V_{Pd}.

For the water-saturated samples, the V_{Ps} measurements range from 4390 to 7300 m s^{-1} (with an average value = 5418 m s^{-1}) (Fig. 5d; Table 1). Water saturation was found to produce an increase in V_{Ps} values and a decrease the V_{Ps} anisotropy. Moreover, the difference between V_{Ps} and V_{Pd} increases as the samples porosity increases. Also, the fractured samples (e.g. PY17_1 and PY17_14) are characterized by a higher difference between V_{Pd} and V_{Ps}.

The V_{Sd} values range from 1790 to 3693 m s^{-1} with an average value of 2540 m s^{-1}. Under the saturated conditions, the V_{Ss} values range from 2145 to 3378 m s^{-1} with an average value of 2643 m s^{-1}. A good linear relationship exists between V_P and V_S as proposed by many researchers for many rock types (e.g. Christensen 2004; Wang *et al.* 2009; Diamantis *et al.* 2011). In this study, the relationship between V_{Sd} and V_{Pd} can be expressed by the equation $V_{Sd} = 0.4408\ V_{Pd} + 388.07$ with $R^2 = 0.812$ as Fig 5c shows.

The TC and V_p measured on dry samples show a positive linear trend (Fig. 4d). This linear relationship has a low correlation coefficient ($R^2 = 0.373$). Since the TC and V_P are sensitive to the same parameters (porosity, mineralogy, saturation, pore shape, fracture filling, etc.) a noticeably different variations occurs (Zamora *et al.* 1993). For example, the fracturing produced a clear decreases in the V_P and an increase of V_P anisotropy of V_p, and it has a low effect at the TC measurement.

4.3.3 Estimating mechanical properties, Young's modulus (E) and Poisson's ratio

Young's modulus (E) and Poisson's ratio (υ) were calculated through V_{Pd}, V_{Sd} and bulk density using the relations $E = \rho(V_p^2 - 2V_s^2)$ and $\nu = (V_p^2 - 2V_s^2)/2(V_p^2 - V_s^2)$, respectively. The results are shown in Table 1. These parameter values range from 20.18 to 117.18 GPa and 0.13 and 0.34 for E and ν respectively. Thus, an increase in porosity and the degree of serpentinization lead to the Young's modulus decreasing logarithmically (Figs 6b and d) even if two different trends can be observed in the Fig. 6(b) for low altered samples (degree of serpentinization <40 per cent) and highly to totally altered samples (degree of serpentinization >40 per cent). The E and ν values are in accordance with published values for different sets of peridotite samples with different grades of alteration (Christensen 1966; Diamantis *et al.* 2011; Kamaci & Özer 2018; Farough & Karrasch 2019). Figs 6(a) and (c) show that no clear relationship seems to exist between the degree of serpentinization

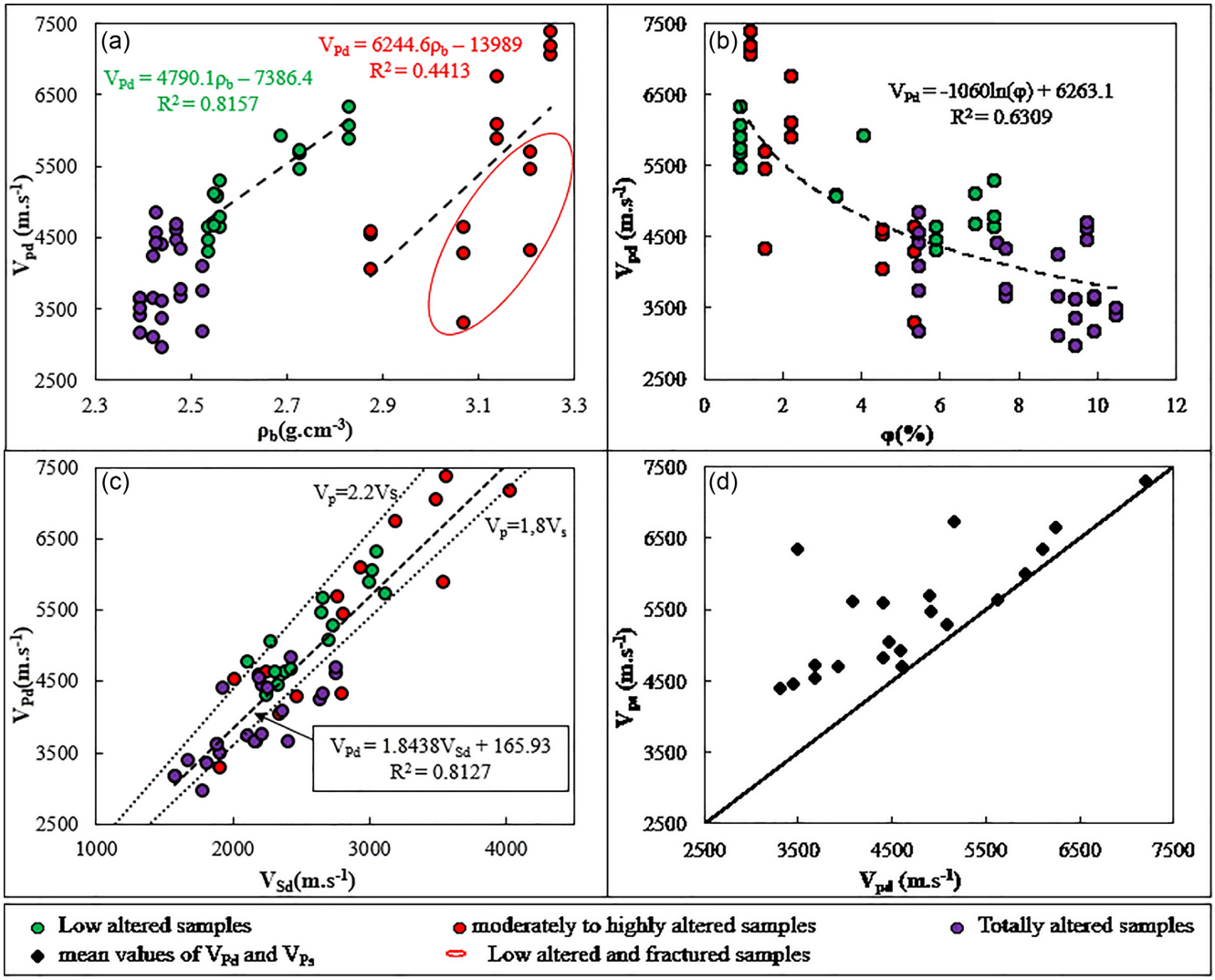

Figure 5. Physical properties of the investigated peridotites: (a) V_{Pd} versus bulk density; (b) V_{Pd} versus porosity; (c) V_{Pd} versus V_{Sd}; (d) mean dry *P*-wave velocity versus mean saturated *P*-wave velocity.

and porosity and Poisson's ratio. However, Christensen (2004) and Farough & Karrasch (2019) have already noted that Poisson's ratio has a tendency to increase as the amount of serpentine in the samples increase (Fig. 6a).

5 DISCUSSION

5.1 Peridotite properties evolution with progressive serpentinization

The serpentinization of peridotite is a phenomenon of progressive transformation of primary minerals. This phenomenon begins with the alteration of olivine minerals followed by the pyroxene minerals. All were transformed to a newly formed phase (usually serpentine). The microscopic observations of the thin sections reveal a major change in mineralogy with serpentinization, especially in the serpentine content. The diminution of the grain and bulk densities is controlled by the replacement of dense minerals such as olivine (3.3 g cm^{-3}) and pyroxene (3.4 g cm^{-3}) with the serpentine (mean density of 2.6 g cm^{-3}). This evolution is illustrated by the samples (PY17_10, PY17_1 and PY17_7) with a low serpentine content (<5 per cent), PY17_3 with 40 per cent serpentine content and the other samples (PY17_24, PY17_20,. . .) with a higher serpentine content (up to 100 per cent). The mineralogical transformation of the altered peridotite goes on with petrophysical properties variation.

The variability of petrophysical properties of the samples characterized in this study gives a first image of the evolution of peridotite properties as a function of serpentinization degree (Fig. 7). The investigated petrophysical properties were found to be strongly influenced by the mineral assemblage and texture of the rock. Further, discontinuities such as microcracks and grain boundaries can impact the V_P and V_S, TC and TD.

In general, our petrographic observations and petrophysical measurements led us to divide the samples into three groups, namely: (1) fresh to low altered samples and (2) moderately to highly altered samples and (3) totally altered samples. The petrophysical properties of the fresh to low altered samples are in phase with the average values for fresh peridotite reported in the literature (~3.2 g cm^{-3}

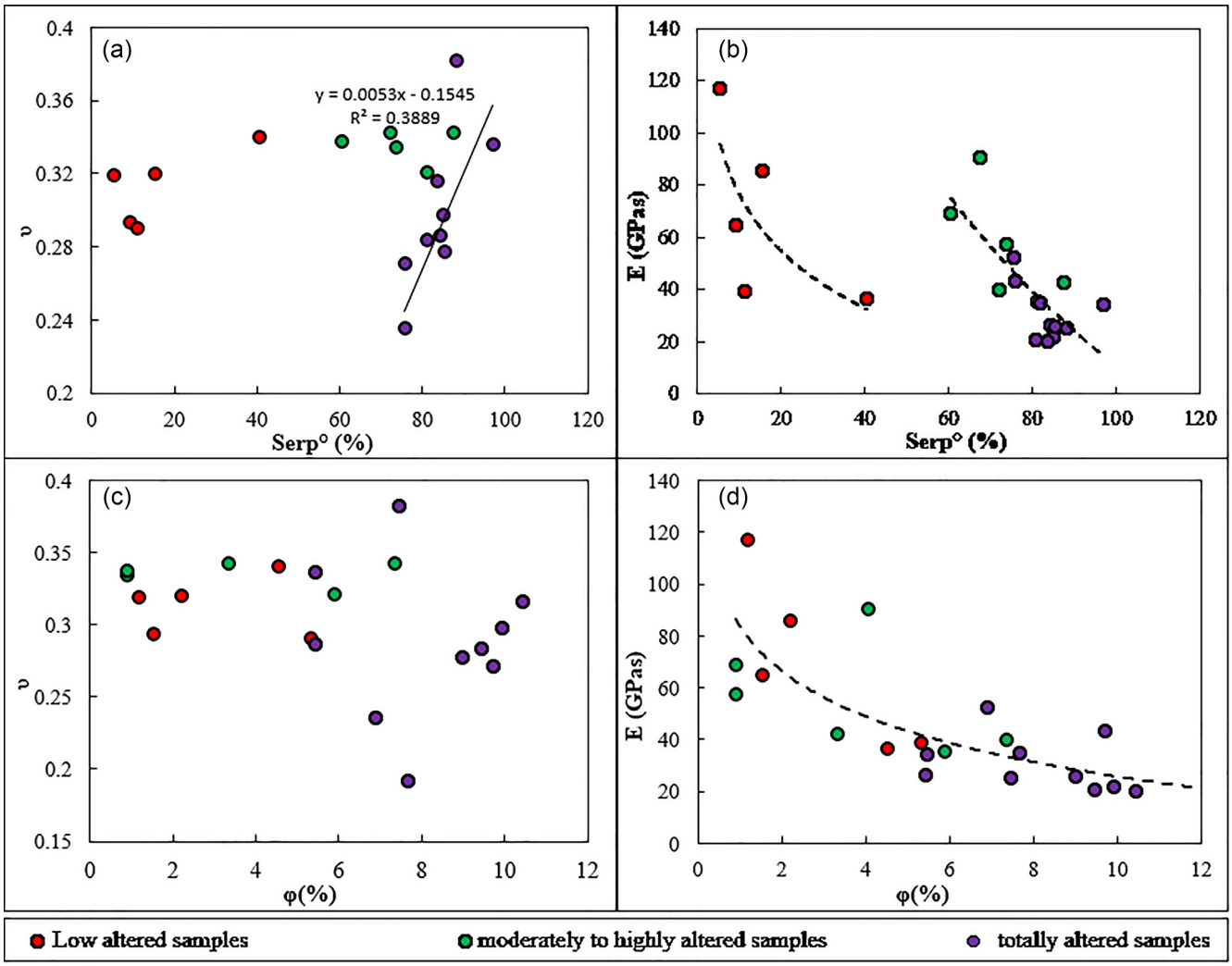

Figure 6. Calculated elastic properties. (a) Poisson ratio versus the degree of serpentinization; (b) Young's modulus versus the degree of serpentinization; (c) Poisson ratio versus porosity; (d) Young's modulus versus porosity.

in solid density, <2.9 per cent in porosity, ∼3.4 W m^{-1} K^{-1} in TC and ∼5400 m s^{-1} in V_{Pd}). Micro and macrocracks cause some variation in porosity and V_P and increase the V_{Pd} anisotropy. The second group has randomly distributed petrophysical properties with an overlap in the first and the third groups. The spread of data reflects the increase in mineralogical and textural complexity resulting from interaction between fresh protolith characteristics and serpentinization processes. The wide variation in the porosity (1 to 7.3 per cent) is interpreted as the effect of the microcracks, fractures, dissolution of primary minerals due to serpentinization, and secondary processes leading to crack and pore sealing. The decrease in the solid density is due to the lower density of serpentine (2.7 g cm^{-3}), which is the principal alteration phase of primary olivine (3.3 g cm^{-3}). V_{Pd} and dry TC spread between 4400 and 6000 m s^{-1} and 1.75 and 2.91 W m^{-1} K^{-1}, respectively and occurred in correlation with the porosity and solid density variations. These variations are the conjoint effect of secondary mineral and textural characteristics (porosity shape, fractures, and pore filling material). The bulk and solid densities of totally altered peridotite became less scattered, and the solid density converged to the mean density of serpentine mineral (2.7 g cm^{-3}). The wide variation in porosity (5–10 per cent), fracture orientation, the shape of pores, and sealing material causes a wide variation of V_P and V_S, TC and TD of the totally altered samples.

Nonetheless, the three groups have some similarities in the amount and types of porosity, V_P, and TC (Fig. 7). Serpentinization increases the porosity of rocks through the development of microcracks and of matrix microporous networks and conversely decreases the solid density (Fig. 7) by the replacement of dense minerals (olivine) with minerals with lower density (serpentine), thus reducing *P*- and *S*-wave velocities and thermal properties (λ and D). The complexity of the texture increases until all the primary phases are altered, then it decreases until complete replacement by serpentine.

5.2 Comparison to the petrophysical data reported in previous studies

The range of solid density measurements illustrates the full range of serpentinite content variations (Figs 3 a and c). This range of variations matched those reported in other studies (Fig. 8; e.g. Gibert 2003; Song *et al.* 2004; Schmitt *et al.* 2007; Diamantis *et al.* 2009, 2011; Iosif Stylianou *et al.* 2016; Falcon-Suarez *et al.* 2017;

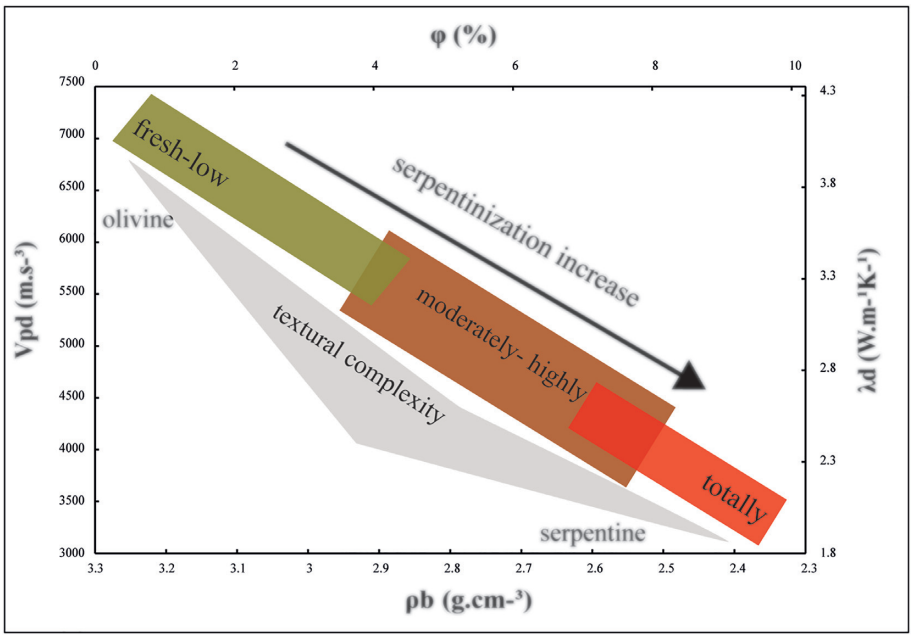

Figure 7. Synthetic diagram model of the petrophysical properties evolution as a function of serpentinization degree of studied peridotite.

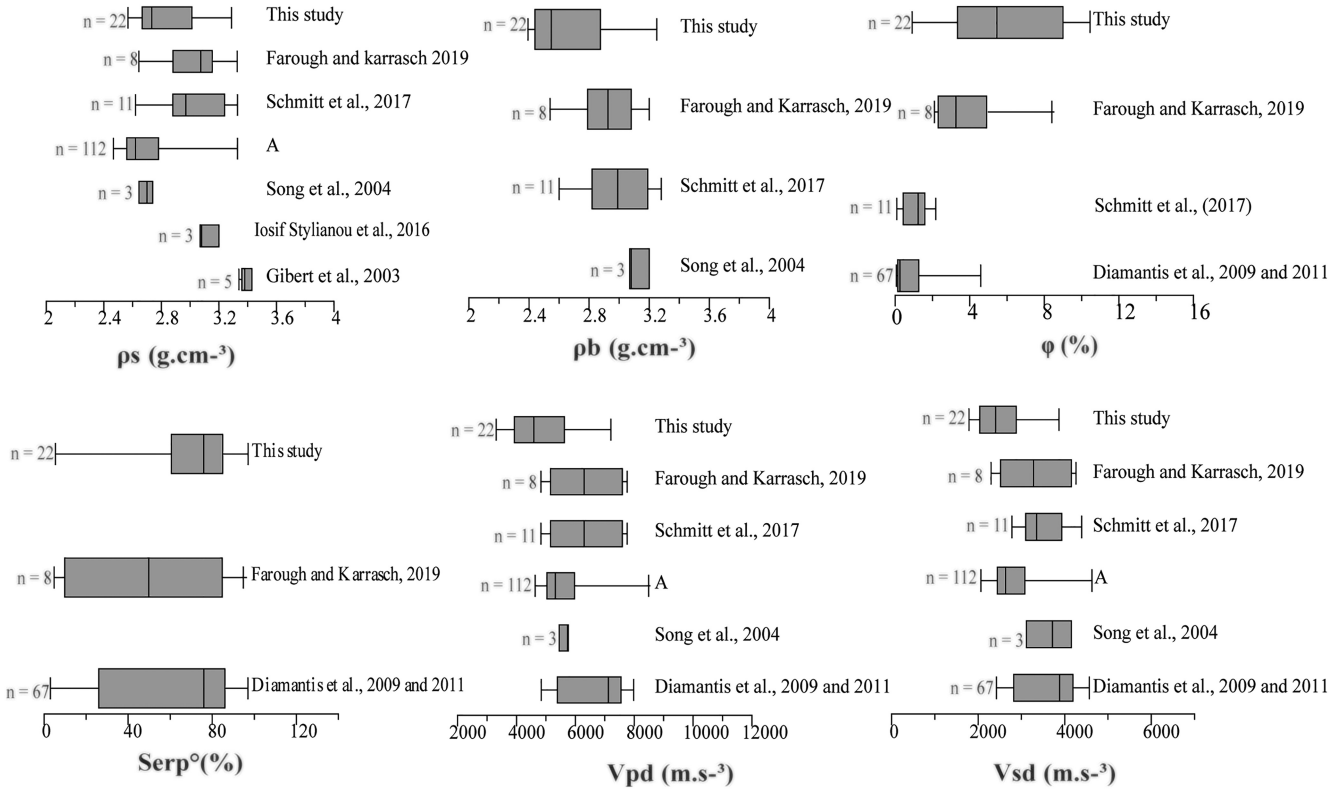

Figure 8. Boxplots of the thermo-physical properties of serpentinized peridotite. Comparison with other published data. (a) Data compiled by Schmitt *et al.* (2007) from different studies. n is the number of samples.

Farough & Karrasch 2019; Manuella & Carbone 2019). For example, Schmitt *et al.* (2007) measured the solid densities of serpentinized ophiolite ranging from 2.62 to 3.3 g cm^{-3} for an equivalent degree of serpentinization ranging between 2.3 and 87.9 per cent. However, most of these studies measured very low porosities (<1 per cent) except Farough & Karrasch (2019) who measured porosities of serpentinized peridotite between 2.1 and 8.4 per cent (Fig. 8); our data set covers all the range of published data.

The range of V_{Pd} and V_{Sd} matched those measured in different locations (Fig. 8; Gibert 2003; Song *et al.* 2004; Schmitt *et al.* 2007; Diamantis *et al.* 2009, 2011; Iosif Stylianou *et al.* 2016; Falcon-Suarez *et al.* 2017; Farough & Karrasch 2019; Manuella & Carbone 2019). Thus, the V_{Pd} and V_{Pd} values measured for the

fresh to slightly altered samples displayed similarities with those measured by Diamantis *et al.* (2009; the ranges of V_{Pd} and V_{Pd} are 7000–8000 and 3800–4550 m s^{-1}, respectively) in samples with lower porosity (<1 per cent) and a low degree of alteration (<30 per cent by volume) from the Central Greece peridotite.

Also, Farough & Karrasch (2019) estimated the V_{Pd} and V_{Sd} of serpentinized peridotite (Fig. 8) in the range of 4834–7759 m s^{-1} for V_{Pd} and 2300–4262 m s^{-1} for V_{Sd} which fits with our measurements. Horen *et al.* (1996) observed a decrease of velocities in serpentinized peridotite of Xigaze ophiolite as the level of serpentinization increases. The V_p and V_s ranged between 5860 and 7760 m s^{-1} and 3080 and 4350 m s^{-1}, respectively, for a degree of serpentinization ranging from 3 to 70 per cent and solid density ranging between 2.7 and 3.2 g cm^{-3}. These velocities are slightly higher due to their lower porosity (between 0.4 and 0.8 per cent) as compared to our Pyrenean peridotite samples.

In contrast, Song et al (2004) measured the mean V_p and V_s between 5200 and 6000 m s^{-1} and 2800 and 3400 m s^{-1}, respectively in three serpentines from the Korean peninsula. The densities of these materials are low (2.64–2 74 g cm^{-3}) and may suggest they are highly serpentinized.

Studies concerning TC and TD measurement under laboratory conditions of different grade serpentinization peridotite are rare, which makes the comparison with our approach (TC and TD evolution as a function of serpentinization) quite complicated. However, numerous data on TC and TD have been reported in the literature. Balkan *et al.* (2017) measured the TC of western Anatolia peridotite and found 2.52 ± 0.45 W m^{-1} K^{-1}. Iosif Stylianou *et al.* (2016) measured TC and TD on ultramafic rocks from Cyprus, TC and TD ranging from 1.7 to 2.9 W m^{-1} K^{-1} and 0.09 to 1.3 mm^2 s^{-1}. Gong (2005) measured for alpine serpentine, and for the dry samples, TC ranges from 2.42 to 3.25 W m^{-1} K^{-1}, and under the saturated condition, TC ranging from 2.44 to 3.32 W m^{-1} K^{-1} for solid density and porosity ranging between 2.66 and 2.87 g cm^{-3} and 0.03 and 0.74 per cent, respectively. Hyndman & Drury's study (1976), of the oceanic basement rocks from deep drilling on the Mid-Atlantic ridge, show that serpentinized peridotites have a TC of 3.19 W m^{-1} K^{-1} and a porosity of 0.8 per cent. He *et al.* (2008) measured mean TCs of 2.97 ± 0.33 W m^{-1} K^{-1} for serpentinite from Chinese Continental Deep Drilling in east China. Thus, the TC and TD of serpentinized peridotite from different regions overall show a wide range of variation (from 1.7 to 3.19 W m^{-1} K^{-1} for TC and 0.09 to 1.3 mm^2 s^{-1} for TD), and data from the present study fall within this range (1.86–4.23 W m^{-1} K^{-1} 0.79–1.58 mm^2 s^{-1} for TC and TD respectively. The wide variation of TC and TD observed from our samples is due to the mineralogical variation between the fresh and totally serpentinized peridotite and the wide variation of the porosity of the samples.

5.3 Thermal conductivity prediction

5.3.1 Thermal conductivity calculated from the mineralogical composition.

In the literature, there are few studies where the TC of crystalline rocks was predicted from their mineralogical composition and porosity and using different mixing models (Horai & Baldridge 1972; Pribnow & Umsonst 1993; Förster *et al.* 2015; Ray *et al.* 2015; Zhao *et al.* 2016; Chopra *et al.* 2018; Fuchs *et al.* 2018; Yu *et al.* 2022), and no studies at all for ultramafic rocks.

Horai & Baldridge (1972) calculated the TC of nineteen igneous rocks samples from the mineralogical and chemical compositions using the Hashin-Shtrikman mean model. Both methods gave satisfactory results. Pribnow & Umsonst (1993) estimated the TC of granitic samples with an absolute mean error of 10 per cent using a geometric mean model. Ray *et al.* (2015) calculated the TC of different types of granulite facies using several mixing models and concluded that the harmonic mean model gives the best fit between calculated and measured TC with an average deviation of −1.2 ± 6 per cent (1σ). Zhao *et al.* (2016) calculated thermal conductivity for water-saturated granitic samples from their mineralogical composition and found that the Hashin–Shtrikman model gives the best fit between calculated and measured TC. Chopra *et al.* (2018) Concluded that the harmonic mean model gives the best fit in the case of low porous granite with an average deviation of 2 ± 8.1 per cent (1σ), using mean mineral TC and mineral composition obtained from modal analysis. Also, the same model gives the best fit (deviation of −1 ± 6 per cent) between measure and calculated TC from modal mineralogy and mean minerals TC for high grade metamorphic rocks with low anisotropy and porosity (Förster *et al.* 2015). Fuchs *et al.* (2018) showed that the use of the harmonic mean model provides a good correlation between the calculated and measured TC for low porous plutonic rocks with an absolute mean error of 1.4 ± 9.7 per cent, and deviation less than 10 per cent using mean mineral TC and mineral composition obtained from modal mineralogy. Fu *et al.* (2019) calculated the TC and TD of four granitoïds (granodiorite, monzogranite, syenogranite, and alkaline granite) by using different mixing models. The authors showed that both the Hashin-Shtrikman upper bound and geometric mean model gave a good fit between measured and calculated TC. In summary, the harmonic, geometric and Hashin-Shtrikman means models seem to be the most relevant for the calculation of the TC of igneous and metamorphic rocks.

This study was carried out to find the best mathematical model (eqs A1–A9) for the indirect calculation of the TC of serpentinized peridotite rocks under dry (Figs 9a and b) and water saturated (Figs 9c and d) conditions from their mineralogical composition and porosity. For this purpose, the mineralogical composition of the samples was obtained by an estimation of the degree of serpentinization (see Section 3.5), and porosity was measured by the triple weighting method.

For dry conditions, the geometric mean model gives the best fit between calculated and measured TC and it gives significantly smallest prediction errors than other models. For λ_{geo}, the deviation between measured and calculated TC varies between −21.5 and 25.7 per cent with an average value of 0.1 ± 14.1 per cent (1σ) and the absolute mean error (AME) is 11.8 ± 7.3 per cent (1σ) (Table 3). The Robertson and Pack models also provide acceptable results with a mean deviation of −6.4 ± 12.4 per cent (1σ) and an absolute mean error of 11.6 per cent ± 7.4 per cent (1σ). All other tested models give poor result and a mean absolute error greater than 17 per cent (between 17.2 and 78.8 per cent; Table 3). For water-saturated conditions, the harmonic mean model gives the best fit between the calculated and measured TC, followed by the Voigt–Reuss–Hill model [mean deviation of 6.6 ± 13.3 per cent (1σ)], the lower bound of the Hashin–Shtrikman mean model [mean deviation of 8.6 ± 13.6 per cent (1σ)], the geometric means model [mean deviation of 10.2 ± 13.5 per cent (1σ)], the Hashin–Shtrikman mean model [mean deviation of 12.0 ± 13.9 per cent (1σ)] and the effective mean model [meann deviation of 13.5 ± 14.1 per cent (1σ)]. The models experimented with give a poor fit between calculated and measured TC with a mean deviation greater than

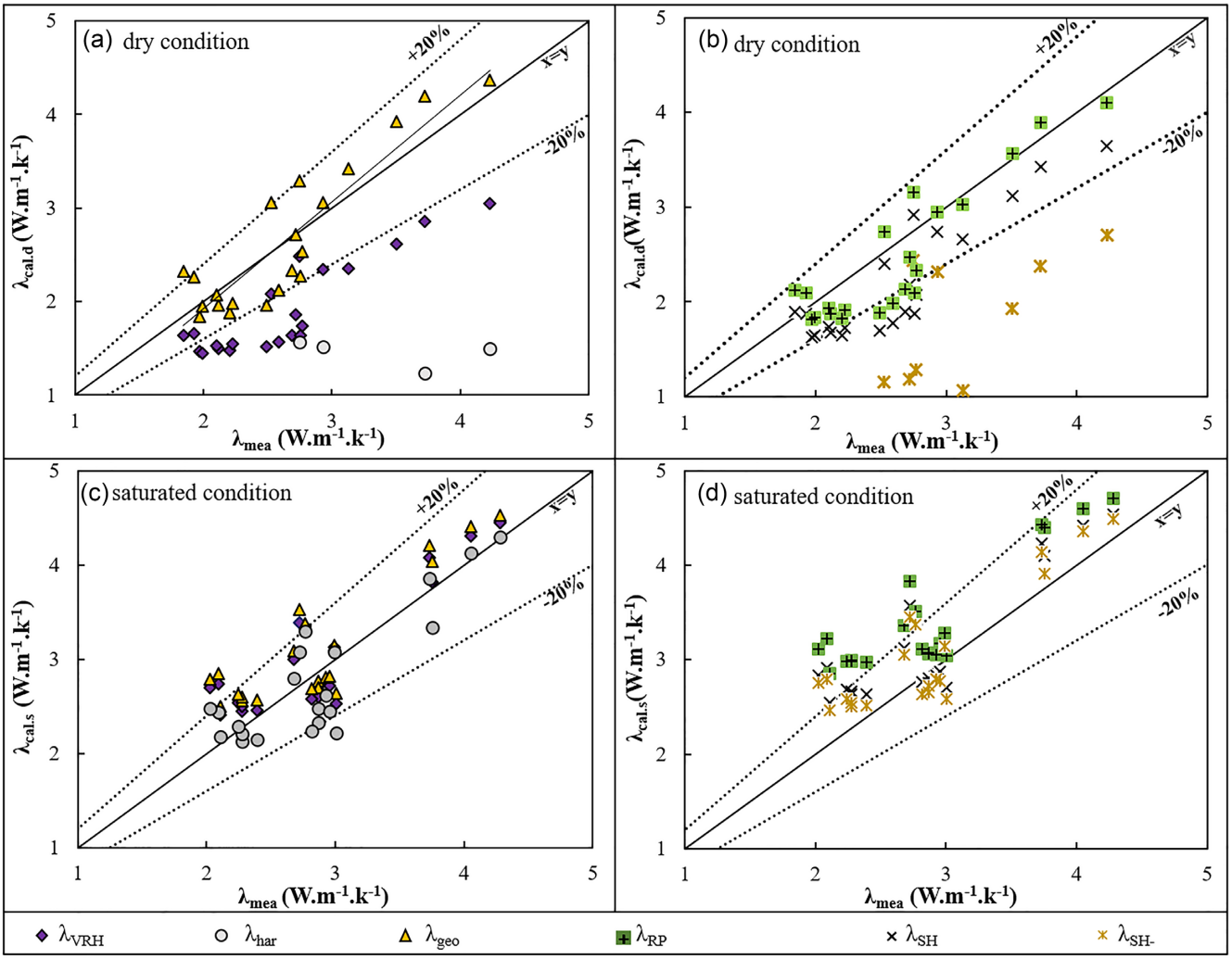

Figure 9. Plot of calculated (λ_{cal}) versus measured (λ_{mea}) bulk thermal conductivities using different mixing models: (a and b) under dry conditions; (c and d) under saturated conditions.

Table 3. Statistical analysis of errors from different mixing model application for prediction of TC under water-saturated and dry conditions. RE, Relative error; AME, absolute mean error; RMSE, root mean square error; σ, standard deviation.

	Dry conditions						Water-saturated conditions					
Model	RE (%)				AME (%)	RMSE (W m^{-1} K^{-1})	RE (%)				AME (%)	RMSE (W m^{-1} K^{-1})
	Min	mean	max	σ (%)			min	mean	max	σ (%)		
λ_{art}	3.4	24.2	56.7	15.7	24.2 ± *15.7*	0.67 ± *0.42*	−5.5	14.9	45.1	14.4	16.3 ± *13.6*	0.51 ± *1.29*
λ_{VRH}	−40.4	27.3	−9.6	9.2	27.3 ± *9.2*	0.78 ± *0.4*	−15.9	6.6	33.3	13.3	11.8 ± *8.8*	0.36 ± *0.15*
λ_{har}	−89.8	−78.9	−43.1	13.1	78.9 ± *13.1*	2.08 ± *1.73*	−26.4	−2.6	22.1	13.4	10.8 ± *7.9*	0.37 ± *0.16*
λ_{geo}	−21.5	0.1	25.7	14.1	11.8 ± *7.3*	0.47 ± *0.28*	14.9	10.2	37.8	13.7	13.5 ± *10.3*	0.41 ± *0.20*
λ_{sqr}	7.0	29.5	63.9	28.5	29.5 ± *17.3*	0.79 ± *0.52*	14.8	38.9	79.8	37.9	39.8 ± *20.2*	0.39 ± *0.17*
λ_{SH-}	4.1	−56.7	35.9	17.9	12.7 ± *17.9*	1.49 ± *1.05*	−14.0	8.6	35.9	13.6	12.7 ± *9.5*	0.39 ± *0.17*
λ_{SH+}	3.4	24.0	56.5	15.6	24.0 ± *15.6*	0.66 ± *0.42*	0.1	16.2	44.9	13.6	16.2 ± *13.6*	0.51 ± *0.42*
λ_{SH}	−32.1	−16.4	6.3	11.2	17.2 ± *9.8*	0.51 ± *0.24*	−9.8	12.0	40.1	13.9	14.2 ± *11.5*	0.51 ± *0.29*
λ_{RP}	−24.3	−6.4	15.3	12.4	11.6 ± *7.4*	0.34 ± *0.14*	1.3	22.0	54.0	15.5	22.0 ± *15.5*	0.65 ± *0.39*
λ_{eff}	1.7	20.3	52.0	14.7	20.3 ± *14.7*	0.5 8 ± *0.36*	−8.2	13.5	41.9	14.1	15.0 ± *12.5*	0.47 ± *0.25*

15 per cent (Table 3). Statistically, the deviation between measured and calculated TC varies between −26.4 and 22.1 per cent, with the average value of −2.4 ± 13.5 per cent (1σ) and the absolute mean error of 10.8 ± 7.9 per cent (1σ) per cent for the harmonic mean model.

For dry conditions, the direction-independent geometric mean model (Lichtenecker 1924) was found to provide the best fit between the measured and calculated TC [standard deviation: 0.09 ± 14.4 per cent (1σ); Fig. 9a; Table 3]. The geometric mean model is an empirical model which assumes a random distribution of mineral

phases and pores (Clauser 2011). Consequently, the absence of any textural pattern, foliation, and layering in studied samples is the reason for the better performance of this model. For water-saturated conditions, the best fit between the measured and calculated TC was unexpectedly achieved by the harmonic mean model (deviation: -2.4 ± 13.4 per cent (1σ); Fig. 7a; Table 3). This result is in agreement with previous studies carried out on igneous and metamorphic rocks (Förster *et al.* 2015; Ray *et al.* 2015; Chopra *et al.* 2018; Fuchs *et al.* 2018; Yu *et al.* 2022). The harmonic mean model is based on a banding model, where the mineral phases are layered perpendicularly to the heat flow (Clauser 2011; Jia *et al.* 2019). Generally, this model is applied to find the lower bound of the TC (Clauser 2011; Jia *et al.* 2019). The reason why this model gives the best performance regardless of the other model's direction-independent is still not entirely clearly understood. However, two hypotheses can be envisaged:

(i) The heat transport through isotropic rock is considerably delayed like a flow perpendicular to stratification in an anisotropic medium due to the countless heat-refraction events caused by the chaotic arrangement of the mineral grains (Fuchs *et al.* 2018; Yu *et al.* 2022). Also, the foliated structure of the serpentine minerals causes heat to be transported in a manner and quantity that are thought to make it perpendicular to the planar boundaries in an anisotropic medium. This effect even greater when the interlayers are filled with water.

(ii) The success of the harmonic model can be also related to the preferred alignment of the fractures in the samples (at the macroscopic and microscopic scales) confirmed by the anisotropy of V_p measurements and by microscopic observations of the thin sections. the sheet structure of serpentine

The divergence between the measured and calculated TC and outliers on model evaluation can be linked to the models themselves, which simplify the complex reality of the rocks so it can be formulated mathematically and analytic measurement errors. However, in our case, the most significant errors may come from accessory mineral phases (pyroxene, spinel and magnetite) that were not accounted for in the TC calculations and also from the use of the mean minerals TC which does not reflect the TC variation because of the solid solution (Jennings *et al.* 2019). Both olivine and serpentine have significant variations in TC as a function of the composition (Table 2). Moreover, the estimation of the volume fraction of each mineral phase of the samples, especially minerals with a large volume fraction can also introduce significant errors in the TC calculation (Jennings *et al.* 2019). Divergences between the measured and calculated TC, outliers and the most performing model might be also related to the impacts of particle size, particle dispersion, pore structure, anisotropy of minerals TC and preferential orientation of the fractures.

While our model presents some uncertainties and limitations, the indirect calculation of TC forms accurate knowledge of peridotite's mineralogical composition, and porosity is demonstrated as a viable option to recover thermal conductivity data with an error of less than 20 per cent. Fig. 10 offers a simple way to estimate dry TC using knowledge the peridotite's porosity and serpentinization degree, or knowing two of them, determine the third.

5.3.2 Estimation of thermal conductivity from empirical models

Thermal conductivity can be also quantified indirectly from the suite of petrophysical properties measured in a laboratory or obtained from well-logging. This kind of approach is based on an analysis of the relationship between TC and other physical properties. Many researchers have studied the correlation of TC of rocks and other single petrophysical proprieties (mineral composition, density and porosity, V_p, and fluid saturation), and the observed correlation trends differ significantly from one to another. Other authors use the statistical methods like multiple linear regression (MLR) to assess the relationships between TC and several properties at the same time (Hartmann *et al.* 2005; Fuchs *et al.* 2013; 2015; Fuchs & Förster 2014; Gąsior & Przelaskowska 2014; Mielke *et al.* 2017). These regression-based empirical equations are also different and typically limited to the rocks which they were based on. In this part, prediction equations for TC (Table 4) were established by multiple linear regression using a set of measured petrophysical properties (porosity, bulk and grain densities and V_{Pd}) and measured TC under dry conditions. The quality of the established regression models was defined by the determination coefficient R^2, standard deviation, RMSE and AME. The sensitivity of the models was examined by removing one or several parameters from the regression while examining and noting any subsequent variations of the misfit (ΔR^2 and ΔRMSE).

In the first, the MLR was performed with four variables (Table 4; eq. 4). The resulting equation from this MLR provides a good level of correlation between measured and calculated TC (Fig. 11). The results have a high correlation coefficient ($R^2 = 0.78$) and an absolute mean error of 9.8 ± 7.0 per cent (1σ). The conductivity of 91 per cent of samples was predicted within absolute errors of less than 20 per cent, while 59 per cent of the samples show a deviation between measured and calculated TC of less than $\pm$ 10 per cent. The variables used to predict TC by this model have individually different relationships with thermal conductivity (Fig. 4).These relationships illustrate the various factors that influence rock TC (mineralogical composition, porosity, texture) The ΔR^2 and ΔRMES from the model 2 (Table 4; eq. 5) show that the apparent density (ρ_b) has very little influence on the TC prediction and can be removed from the prediction model. In fact, the reduction of the model to the three predictor variables (porosity, solid density, and V_{pd}) results in an insignificant increase in AME (ΔAME $= 0.1$ per cent). The thermal conductivity of more than 45 per cent of the samples was predicted with an AME of less than 10 per cent (Fig. 11). An accurate calculated TC was also obtained by using just two predictor variables: porosity and solid (Table 4, eq. 6) or solid density and V_{pd} (Table 4, eq. 8). The AME and the determination confidents resulting from these models (Table 4) indicate a good degree of tracking. Compared to the first model (eq .4), the misfit resulting from the reduction of the model to two prediction variables is insignificant for the applications.

Interestingly, Fig. 11 shows that the four most effective models provided by the MLR method (eqs 4 to 8) give almost the same results. The application of one of these equations allows the prediction of the TC with an acceptable level of error (AME less the 20 per cent). Moreover, although the four most effective models provided by the MLR method cannot predict the TC of peridotite perfectly, they perform well compared to the geometric mean model (Table 4; Fig. 11) which gives the best fit between measured and calculated dry TC in the mineralogy model. The geometric mean model only enables the prediction of the TC of 81 per cent of the samples with an AME below 20 per cent and TC of 40 per cent of the samples with an AME lower than 10 per cent. In addition, the correlation-based models performed using the MLR method are easily applied to existing data sets collected from

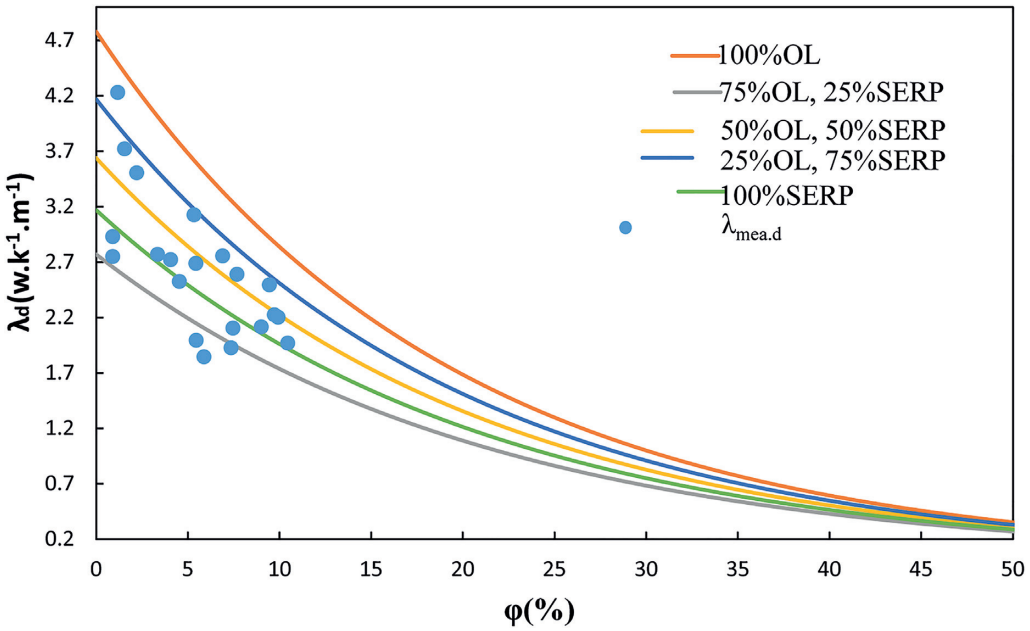

Figure10. Thermal conductivity calculation from the geometric mean model as a function of porosity and serpentinization degree. The porosity thermal conductivity trend established in our study is shown with blue circle.

Table 4. Equations derived from the multiple linear regression analysis for thermal conductivity prediction. R^2, determination coefficient; AME, absolute mean error; RMSE, root mean square error. The ΔRMSE end ΔR^2 are calculated as the RMSE and R^2 of model 1 minus RMSE and R^2 of *i*th model.

Model	TC prediction equations	R^2	ΔR^2	AME (%)	RMSE (W m^{-1} K^{-1})	ΔRMSE (W m^{-1} K^{-1})	Eq.
1	$\lambda = -0.087\varphi + 3.147\rho_s + 6.932 \times 10^{-5}\, V_{Pd} - 1.464\rho_b - 2.185$	0.78	–	9.8 ± *7.0*	0.29 ± *0.09*	–	(4)
2	$\lambda = -0.055\varphi + 1.721\rho_s + 4.624 \times 10^{-5} V_{Pd} - 2.1500$	0.77	0.01	9.6 ± *7.6*	0.29 ± *0.09*	0	(5)
3	$\lambda = -0.063\varphi + 1.717\rho_s - 1.857$	0.75	0.03	9.6 ± *7.7*	0.30 ± *0.10*	0.01	(6)
4	$\lambda = -0.107\varphi + 1.089 \times 10^{-4} V_{Pd} + 2.6912$	0.49	0.29	12.5 ± *8.1*	0.42 ± *0.21*	0.13	(7)
5	$\lambda = 1.647 \times 10^{-4} V_{Pd} + 0.860\rho_s - 3.409$	0.75	0.04	10.1 ± *7.6*	0.30 ± *0.10*	0.01	(8)
	$\lambda_{geo} = \prod_{i=1}^{n} \lambda_i^{xi}$	0.8	−0.02	11.81 ± *7.32*	0.47 ± *0.28*	0.18	(9)

the well-log or laboratory without the need for laboratory time-consuming measurements. On the other hand, it enables the prediction of the TC from well-log data for which samples are not accessible. The MLR models are constructed from petrophysical data that are commonly collected by industry and researchers around the world.

6 CONCLUSION

The petrophysical properties (porosity, density, TC, TD, *P*-wave velocity, *S*-wave velocity) and petrographic composition of 22 peridotite samples were investigated in the laboratory. These data are all necessary to improve statistical confidence in input data in earth geophysical and numerical models. After that, we calculated TC from the mineralogical model using mathematical mixing models and from the empirical relationships constructed by the MLR method. Then we compared the calculated and measured TCs. Based on this study, the main conclusions are:

(i) The data set acquired in this study indicates that the major serpentinization processes gradually replaced olivine, pyroxene and spinel minerals with a new-formed serpentine. The mechanical and mineralogical changes brought about by serpentinization were found to induce changes to petrophysical properties in the studied samples. The key indicators of serpentinization from petrophysical properties in peridotite include the increase of porosity up to 10 per cent associated with a clear decrease in the solid density from 3.29 g cm^{-1} for fresh peridotite to 2.5 g cm^{-3} for totally serpentinized ones. The thermo-physical properties follow the same decreasing trend as the serpentinization increases up to 3000 m s^{-1} and 1.85 W m^{-1} K^{-1} for *P*-wave velocity and TC, respectively. Additionally, two groups were defined according to the degree of alteration of the samples: (I) Fresh to slightly altered samples were composed mainly of low altered olivine and fresh pyroxene. The porosity of these samples ranged between 1 to 5 per cent with an average of 2.5 per cent, the solid density was between 3.01 and 3.29 g cm^{-1}, V_{pd} ranged from 3300 to 7200 m s^{-1} and the TC varied between 2.5 and 4.2 W m^{-1} K^{-1}. (II) The moderately to totally altered samples were mainly composed of serpentine. These samples show a wide variation in petrophysical proprieties due to the heterogeneous distribution of various primary and secondary mineral phases and their pore network made up of fracture and microcracks. The porosity of the moderately to totally altered samples ranged from 1 to 10 per cent, the solid density between 2.5 and 2.8 g cm^{-3} while the *V*p

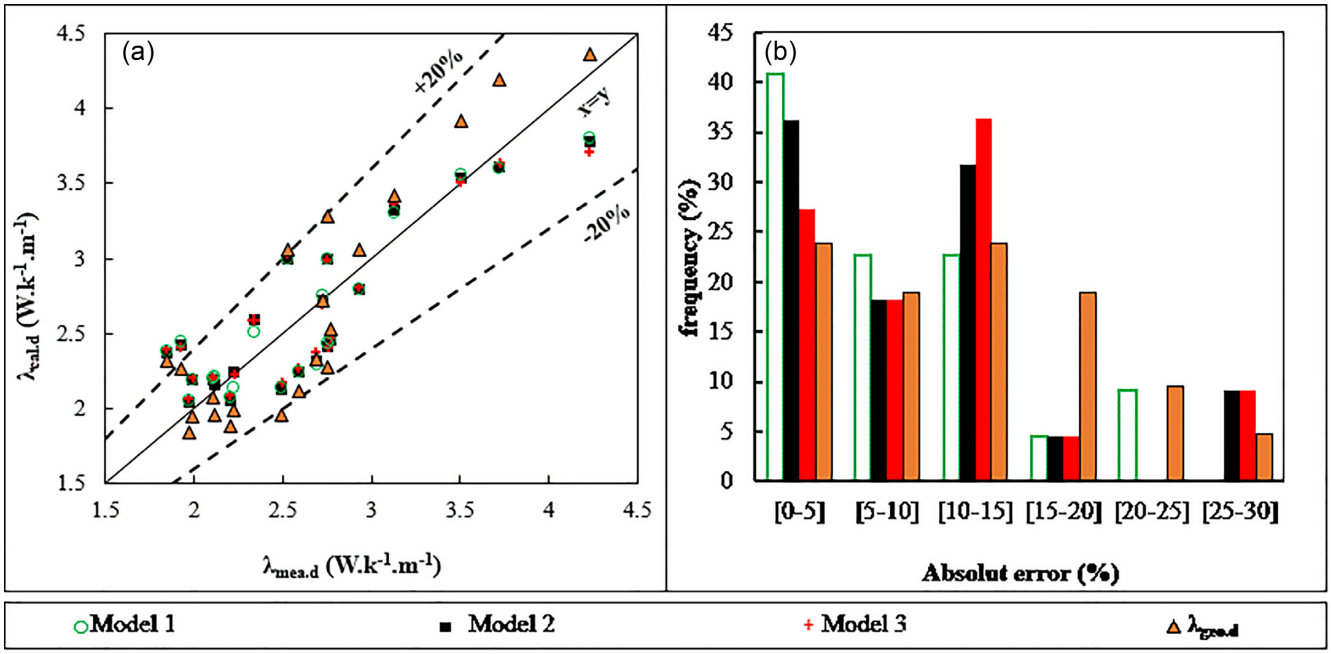

Figure 11. (a) plot of calculated TC ($\lambda_{cal.d}$) versus measured TC ($\lambda_{mea.d}$). (b) Diagram showing the distribution of the absolute errors between $\lambda_{mea.d}$ and $\lambda_{cal.d}$ from different empirical relationships and geometric mean model.

and TC were found to be less than 6000 m s^{-1} and 2.7 W m^{-1} K^{-1} respectively.

(ii) Thermal conductivity calculated from mineralogical composition using different mixing models showed that the geometric means model gives the best fit between measured and calculated thermal conductivities under dry conditions (AME = 11.8 ± 7 per cent (1σ)), while the harmonic model provides a good approximation of the thermal conductivity under saturated conditions (AME = 10.8 ± 7.9 per cent (1σ)).

(iii) The empirical models performed using MLR between the thermal conductivity and other laboratory-measured petrophysical parameters (porosity, densities, and V_p) can predict the thermal conductivity of serpentinized peridotite with an average error of 10 per cent.

(iv) The MLR models, especially model 1 (eq 4), provide a better approximation of thermal conductivity than the geometric mean model. A model constructed from MLR means that TC can be estimated from any data set containing petrophysical properties without having any core samples.

AVAILABILITY OF DATA

The data underlying this article are available in the OTELo research data repository https://ordar.otelo.univ-lorraine.fr: [https://doi.org/10.24396/ORDAR-87; https://doi.org/10.24396/ORDAR-94; https://doi.org/10.24396/ORDAR-95; https://doi.org/10.24396/ORDAR-96; https://doi.org/10.24396/ORDAR-97]

ACKNOWLEDGMENTS

Authors would like to thank Prof. Juan Carlos Afonso, Editor-in-Chief, Prof. Louise Alexander, Assistant Editor, and the two capable reviewers for their keen interest, valuable comments on the manuscript and improvements to this work.

REFERENCES

Abdulagatova, Z., Abdulagatov, I.M. & Emirov, V.N., 2009. Effect of temperature and pressure on the thermal conductivity of sandstone, *Int. J. Rock Mech. Min. Sci.,* **46,** 1055–1071.

Albert, K., Franz, C., Koenigsdorff, R. & Zosseder, K., 2017. Inverse estimation of rock thermal conductivity based on numerical microscale modeling from sandstone thin sections, *Eng. Geol.,* **231,** 1–8.

Bach, W., Garrido, C.J., Paulick, H., Harvey, J. & Rosner, M., 2004. Seawater-peridotite interactions: first insights from ODP Leg 209, MAR 15° N: seawater-peridotite interactions, *Geochem. Geophys. Geosystems,* **5,** https://doi:10.1029/2004GC000744.

Balkan, E., Erkan, K. & Şalk, M., 2017. Thermal conductivity of major rock types in western and central Anatolia regions, Turkey, *J. Geophys. Eng.,* **14,** 909–919.

Beaumont, C., Muñoz, J.A., Hamilton, J. & Fullsack, P., 2000. Factors controlling the Alpine evolution of the central Pyrenees inferred from a comparison of observations and geodynamical models, *J. geophys. Res.,* **105,** 8121–8145.

Beck, A.E., Darbha, D.M. & Schloessin, H.H., 1978. Lattice conductivities of single-crystal and polycrystalline materials at mantle pressures and temperatures, *Phys. Earth planet. Inter.,* **17,** 35–53.

Bertrand, L., Géraud, Y. & Diraison, M., 2021. Petrophysical properties in faulted basement rocks: insights from outcropping analogues on the West European Rift shoulders, *Geothermics,* **95,** 102144.

Birch, F. & Clark, H., 1940. The thermal conductivity of rocks and its dependence upon temperature and composition; Part II, *Am. J. Sci.,* **238,** 613–635.

Boillot, G. *et al.*, 1987. Tectonic denudation of the upper mantle along passive margins: a model based on drilling results (ODP leg 103, western Galicia margin, Spain), *Tectonophysics,* **132,** 335–342.

Boulanouar, A., Rahmouni, A., Boukalouch, M., Samaouali, A., Géraud, Y., Harnafi, M. & Sebbani, J., 2013. Determination of thermal conductivity and porosity of building Stone from ultrasonic velocity measurements, *Geomaterials,* **03,** 138–144.

Bourbié, T., Coussy, O. & Zinszer, B., 1986. Acoustiques des milieux poreux, *IFP,* **27,** 339p.

Chang, Y.-Y., Hsieh, W.-P., Tan, E. & Chen, J., 2017. Hydration-reduced lattice thermal conductivity of olivine in Earth's upper mantle, *Proc. Natl. Acad. Sci. USA,* **114,** 4078–4081.

Chekhonin, E. *et al.*, 2021. Advanced methods of thermal petrophysics as a means to reduce uncertainties during thermal EOR modeling of unconventional reservoirs, *Geosciences,* **11,** 203.

Chopra, N., Ray, L., Satyanarayanan, M. & Elangovan, R., 2018. Evaluate best-mixing model for estimating thermal conductivity for granitoids from mineralogy: a case study for the granitoids of the Bundelkhand craton, central India, *Geothermics,* **75,** 1–14.

Choukroune, P., 1989. The Ecors Pyrenean deep seismic profile reflection data and the overall structure of an orogenic belt, *Tectonics,* **8,** 23–39.

Choukroune, P., 1992. Tectonic evolution of the Pyrénées, *Annu. Rev. Earth Planet. Sci.,* **20,** 143–158.

Christensen, N.I., 1966. Elasticity of ultrabasic rocks, *J. geophys. Res.,* **71,** 5921–5931.

Christensen, N.I., 2004. Serpentinites, peridotites, and seismology, *Int. Geol. Rev.,* **46,** 795–816.

Clauser, C., 2009. Heat transport processes in the earth's crust, *Surv. Geophys.,* **30,** 163–191.

Clauser, C., 2011. Thermal storage and transport properties of rocks, II: thermal conductivity and diffusivity, in *Encyclopedia of Solid Earth Geophysics Encyclopedia of Earth Sciences Series,* ed. Gupta, H.K., pp. 1431–1448, Springer Netherlands.

Clauser, C., 2021. Thermal storage and transport properties of rocks, II: thermal conductivity and diffusivity, in *Encyclopedia of Solid Earth Geophysics Encyclopedia of Earth Sciences Series,* ed. Gupta, H.K., pp. 1769–1787, Springer International Publishing.

Clauser, C. & Huenges, E., 2013. Thermal conductivity of rocks and minerals, in *AGU Reference Shelf,* ed. Ahrens, T.J., pp. 105–126, American Geophysical Union.

Clauser, C. *et al.*, 1997. The thermal regime of the crystalline continental crust: implications from the KTB, *J. geophys. Res.,* **102,** 18417–18441.

Clerc, C., Lagabrielle, Y., Neumaier, M., Reynaud, J.-Y. & Saint Blanquat, M. de., 2012. Exhumation of subcontinental mantle rocks: evidence from ultramafic-bearing clastic deposits nearby the Lherz peridotite body, French Pyrenees, *Bull. Soc. Géol. Fr.,* **183,** 443–459.

Deo, M., Roehner, R., Allis, R. & Moore, J., 2014. Modeling of geothermal energy production from stratigraphic reservoirs in the Great Basin, *Geothermics,* **51,** 38–45.

Diamantis, K., Gartzos, E. & Migiros, G., 2009. Study on uniaxial compressive strength, point load strength index, dynamic and physical properties of serpentinites from Central Greece: test results and empirical relations, *Eng. Geol.,* **108,** 199–207.

Diamantis, K., Bellas, S., Migiros, G. & Gartzos, E., 2011. Correlating wave velocities with physical, mechanical properties and petrographic characteristics of peridotites from the Central Greece, *Geotech. Geol. Eng.,* **29,** 1049–1062.

Diamantis, K., Gartzos, E. & Migiros, G., 2014. Influence of petrographic characteristics on physico-mechanical properties of ultrabasic rocks from central Greece, *Bull. Eng. Geol. Environ.,* **73,** 1273–1292.

Dobson, D.P., Hunt, S.A., McCormack, R., Lord, O.T., Weidner, D.J., Li, L. & Walker, A.M., 2010. Thermal diffusivity of MORB-composition rocks to 15 GPa: implications for triggering of deep seismicity, *High Press. Res.,* **30,** 406–414.

Duretz, T., Schmalholz, S.M., Podladchikov, Y.Y. & Yuen, D.A., 2014. Physics-controlled thickness of shear zones caused by viscous heating: implications for crustal shear localization, *Geophys. Res. Lett.,* **41,** 4904–4911.

Esteban, L., Pimienta, L., Sarout, J., Piane, C.D., Haffen, S., Geraud, Y. & Timms, N.E., 2015. Study cases of thermal conductivity prediction from P-wave velocity and porosity, *Geothermics,* **53,** 255–269.

Fabriès, J., Lorand, J.-P. & Bodinier, J.-L., 1998. Petrogenetic evolution of orogenic lherzolite massifs in the central and western Pyrenees, *Tectonophysics,* **292,** 145–167.

Falcon-Suarez, I., Bayrakci, G., Minshull, T.A., North, L.J., Best, A.I. & Rouméjon, S., & IODP Expedition 357 Science Party, 2017. Elastic and electrical properties and permeability of serpentinites from Atlantis Massif, Mid-Atlantic Ridge, *Geophys. J. Int.,* **211,** 686–699.

Farough, A. & Karrasch, A.K., 2019. Correlation of elastic moduli and serpentine content in ultramafic rocks, *Geosciences,* **9,** 494.

Ford, M., Hemmer, L., Vacherat, A., Gallagher, K. & Christophoul, F., 2016. Retro-wedge foreland basin evolution along the ECORS line, eastern Pyrenees, France, *J. Geol. Soc.,* **173,** 419–437.

Förster, A., Labani, R., Förster, H. -J. & Fuchs, S., 2015. Measured versus calculated thermal conductivity of high-grade metamorphic rocks – inferences on the thermal properties of the lower crust at ambient and in-situ conditions, Unpublished. https://doi:10.13140/RG.2.1.3977.2649.

Fu, H., Zhang, B., Ge, J., Xiong, Z., Zhai, S., Shan, S. & Li, H., 2019. Thermal diffusivity and thermal conductivity of granitoids at 283–988 K and 0.3–1.5 GPa, *Am. Mineral.,* **104,** 1533–1545.

Fuchs, S. & Förster, A., 2010. Rock thermal conductivity of Mesozoic geothermal aquifers in the Northeast German Basin, *Geochemistry,* **70,** 13–22.

Fuchs, S. & Förster, A., 2014. Well-log based prediction of thermal conductivity of sedimentary successions: a case study from the North German Basin, *Geophys. J. Int.,* **196,** 291–311.

Fuchs, S., Schütz, F., Förster, H.-J. & Förster, A., 2013. Evaluation of common mixing models for calculating bulk thermal conductivity of sedimentary rocks: correction charts and new conversion equations, *Geothermics,* **47,** 40–52.

Fuchs, S., Balling, N. & Förster, A., 2015. Calculation of thermal conductivity, thermal diffusivity and specific heat capacity of sedimentary rocks using petrophysical well logs, *Geophys. J. Int.,* **203,** 1977–2000.

Fuchs, S., Förster, H. -J., Braune, K. & Förster, A., 2018. Calculation of thermal conductivity of low-porous, isotropic plutonic rocks of the crust at ambient conditions from modal mineralogy and porosity: a viable alternative for direct measurement?,*J. geophys. Res.,* **123,** 8602–8614.

Garcia, A.V. & Santamarina, J.C., 2021. Heat flow in fractured rocks: stress and moisture-dependent thermal contact resistance, *Geothermics,* **95,** 102113.

Gąsior, I. & Przelaskowska, A., 2014. Estimating thermal conductivity from core and well log data, *Acta Geophys.*, **62,** 785–801.

Ge, J., Zhang, B., Xiong, Z., He, L. & Li, H., 2021. Thermal properties of harzburgite and dunite at 0.8–3 GPa and 300–823 K and implications for the thermal evolution of Tibet, *Geosci. Front.,* **12,** 947–956.

Gegenhuber, N. & Schoen, J., 2012. New approaches for the relationship between compressional wave velocity and thermal conductivity, *J. Appl. Geophys.,* **76,** 50–55.

Gibert, B., 2003. Thermal diffusivity of upper mantle rocks: influence of temperature, pressure, and the deformation fabric, *J. Geophys. Res.,* **108,** 2359.

Gong, G., 2005. *Physical properties of alpine rocks : a laboratory investigation,* Université de Genève. doi:10.13097/archive-ouverte/unige:371.

Goutorbe, B., Lucazeau, F. & Bonneville, A., 2006. Using neural networks to predict thermal conductivity from geophysical well logs, *Geophys. J. Int.,* **166,** 115–125.

Grevemeyer, I., Kaul, N., Villinger, H. & Weigel, W., 1999. Hydrothermal activity and the evolution of the seismic properties of upper oceanic crust, *J. geophys. Res.,* **104,** 5069–5079.

Gu, Y., Rühaak, W., Bär, K. & Sass, I., 2017. Using seismic data to estimate the spatial distribution of rock thermal conductivity at reservoir scale, *Geothermics,* **66,** 61–72.

Haffen, S., Geraud, Y., Diraison, M. & Dezayes, C., 2013. Determination of fluid-flow zones in a geothermal sandstone reservoir using thermal conductivity and temperature logs, *Geothermics,* **46,** 32–41.

Haffen, S., Géraud, Y., Rosener, M. & Diraison, M., 2017. Thermal conductivity and porosity maps for different materials: a combined case study of granite and sandstone, *Geothermics,* **66,** 143–150.

Hartmann, A., Rath, V. & Clauser, C., 2005. Thermal conductivity from core and well log data, *Int. J. Rock Mech. Min. Sci.,* **42,** 1042–1055.

He, L., Hu, S., Huang, S., Yang, W., Wang, J., Yuan, Y. & Yang, S., 2008. Heat flow study at the Chinese Continental Scientific Drilling site: borehole temperature, thermal conductivity, and radiogenic heat production, *J. geophys. Res.,* **113,** B02404. https://doi:10.1029/2007JB004958.

Hieronymus, C.F. & Goes, S., 2010. Complex cratonic seismic structure from thermal models of the lithosphere: effects of variations in deep radiogenic heating, *Geophys. J. Int.,* **180,** 999–1012.

Horai, K., 1971. Thermal conductivity of rock-forming minerals, *J. geophys. Res.,* **76,** 1278–1308.

Horai, K. & Simmons, G., 1969. Thermal conductivity of rock-forming minerals, *Earth planet. Sci. Lett.,* **6,** 359–368.

Horai, K.-I. & Baldridge, S., 1972. Thermal conductivity of nineteen igneous rocks, II estimation of the thermal conductivity of rock from the mineral and chemical compositions, *Phys. Earth planet. Inter.,* **5,** 157–166.

Horen, H., Zamora, M. & Dubuisson, G., 1996. Seismic waves velocities and anisotropy in serpentinized peridotites from xigaze ophiolite: abundance of serpentine in slow spreading ridge, *Geophys. Res. Lett.,* **23,** 9–12.

Hyndman, R.D. & Drury, M.J., 1976. The physical properties of oceanic basement rocks from deep drilling on the Mid-Atlantic Ridge, *J. geophys. Res.,* **81,** 4042–4052.

Iosif Stylianou, I., Tassou, S., Christodoulides, P., Panayides, I. & Florides, G., 2016. Measurement and analysis of thermal properties of rocks for the compilation of geothermal maps of Cyprus, *Renewable Energy,* **88,** 418–429.

Jacobsen, S.D., Jiang, F., Mao, Z., Duffy, T.S., Smyth, J.R., Holl, C.M. & Frost, D.J., 2008. Effects of hydration on the elastic properties of olivine, *Geophys. Res. Lett.,* **35,** L14303. https://doi:10.1029/2008GL034398.

Jammes, S., Manatschal, G., Lavier, L. & Masini, E., 2009. Tectonosedimentary evolution related to extreme crustal thinning ahead of a propagating ocean: example of the western Pyrenees: extreme crustal thinning in the Pyrenees, *Tectonics,* **28**. https://doi:10.1029/2008TC002406.

Jennings, S., Hasterok, D. & Payne, J., 2019. A new compositionally based thermal conductivity model for plutonic rocks, *Geophys. J. Int.,* **219,** 1377–1394.

Jia, G.S., Tao, Z.Y., Meng, X.Z., Ma, C.F., Chai, J.C. & Jin, L.W., 2019. Review of effective thermal conductivity models of rock-soil for geothermal energy applications, *Geothermics,* **77,** 1–11.

Jorand, R., Vogt, C., Marquart, G. & Clauser, C., 2013. Effective thermal conductivity of heterogeneous rocks from laboratory experiments and numerical modeling: thermal conductivity of rocks, *J. geophys. Res.,* **118,** 5225–5235.

Jorand, R., Clauser, C., Marquart, G. & Pechnig, R., 2015. Statistically reliable petrophysical properties of potential reservoir rocks for geothermal energy use and their relation to lithostratigraphy and rock composition: the NE Rhenish Massif and the Lower Rhine Embayment (Germany), *Geothermics,* **53,** 413–428.

Kamaci, Z. & Özer, P., 2018. Engineering properties of Eğirdir-Kızıldağ harzburgitic peridotites in southwestern Turkey, *Int. J. Comput. Exp. Sci. Eng.,* **4,** 14–22.

Kanamori, H., Fujii, N. & Mizutani, H., 1968. Thermal diffusivity measurement of rock-forming minerals from 300° to 1100°K, *J. geophys. Res.,* **73,** 595–605.

Karson, J.A., Cannat, M., Miller, D.J. & Elthon, D.(Eds.)., 1997. *Proceedings of the Ocean Drilling Program, 153 Scientific Results,*Ocean Drilling Program.

Katayama, I. *et al.*, 2020. Permeability profiles across the crust-mantle sections in the oman drilling project inferred from dry and wet resistivity data, *J. geophys. Res.,* **125**. https://doi:10.1029/2019JB018698.

Krzeminska, D.M., Steele-Dunne, S.C., Bogaard, T.A., Rutten, M.M., Sailhac, P. & Geraud, Y., 2012. High-resolution temperature observations to monitor soil thermal properties as a proxy for soil moisture condition in clay-shale landslide, *Hydrol. Process.,* **26,** 2143–2156.

Lagabrielle, Y. & Bodinier, J.-L., 2008. Submarine reworking of exhumed subcontinental mantle rocks: field evidence from the Lherz peridotites, French Pyrenees: cretaceous exhumation of Pyrenean mantle, *Terra Nova,* **20,** 11–21.

Lagabrielle, Y., Labaume, P. & Saint Blanquat, M. de., 2010. Mantle exhumation, crustal denudation, and gravity tectonics during Cretaceous rifting in the Pyrenean realm (SW Europe): insights from the geological setting of the lherzolite bodies: pyrenean lherzolites, gravity tectonics, *Tectonics,* **29**. https://doi:10.1029/2009TC002588.

Lichtenecker, K., 1924. Der elektrische Leitungswiderstand künstlicher und natürlicher Aggregate, *Phys. Z.,* **25,** 226–233.

Manuella, F.C. & Carbone, S., 2019. The identity of petrophysical properties of oceanic serpentinites and continental granitoids: implications for the recognition of buried hydrocarbon-bearing serpentinite geobodies, *Geotectonics,* **53,** 239–250.

Mckenzie, D., Jackson, J. & Priestley, K., 2005. Thermal structure of oceanic and continental lithosphere, *Earth planet. Sci. Lett.,* **233,** 337–349.

Mielke, P., Bär, K. & Sass, I., 2017. Determining the relationship of thermal conductivity and compressional wave velocity of common rock types as a basis for reservoir characterization, *J. Appl. Geophys.,* **140,** 135–144.

Miller, D. J. & Christensen, N. I., 1997. Seismic velocities of lower crustal and upper mantle rocks form the slow-spreading Mid-Atlantic Ridge, South of the Kane transform zone (MARK), in *Proceedings of the Ocean Drilling Program, 153 Scientific Results,* eds Karson, J. A., Cannat, M., Miller, D. J. & Elthon, D., pp. 437–454, Ocean Drilling Program.

Minnigh, L.D., Calsteren, P.W.C. van & Tex, E. den., 1980. Quenching: an additional model for emplacement of the Iherzolite at Lers (French Pyrenees), *Geology,* **8,** 18.

Moore, D.E., Lockner, D.A. & Hickman, S., 2016. Hydrothermal frictional strengths of rock and mineral samples relevant to the creeping section of the San Andreas Fault, *J. Struct. Geol.,* **89,** 153–167.

Mottaghy, D. *et al.*, 2005. New heat flow data from the immediate vicinity of the Kola super-deep borehole: vertical variation in heat flow confirmed and attributed to advection, *Tectonophysics,* **401,** 119–142.

Mouthereau, F. *et al.*, 2014. Placing limits to shortening evolution in the Pyrenees: role of margin architecture and implications for the Iberia/Europe convergence: plate convergence in the Pyrenees, *Tectonics,* **33,** 2283–2314.

Navelot, V. *et al.*, 2018. Petrophysical properties of volcanic rocks and impacts of hydrothermal alteration in the Guadeloupe Archipelago (West Indies), *J. Volc. Geotherm. Res.,* **360,** 1–21.

Ohtani, E., 2020. The role of water in Earth's mantle, *Natl. Sci. Rev.,* **7,** 224–232.

Omodeo-Salé, S., Eruteya, O.E., Cassola, T., Baniasad, A. & Moscariello, A., 2020. A basin thermal modelling approach to mitigate geothermal energy exploration risks: the St. Gallen case study (eastern Switzerland), *Geothermics,* **87,** 101876.

Özkahraman, H.T., Selver, R. & Işık, E.C., 2004. Determination of the thermal conductivity of rock from P-wave velocity, *Int. J. Rock Mech. Min. Sci.,* **41,** 703–708.

Pimienta, L., Sarout, J., Esteban, L. & Piane, C.D., 2014. Prediction of rocks thermal conductivity from elastic wave velocities, mineralogy and microstructure, *Geophys. J. Int.,* **197,** 860–874.

Popov, Y., Beardsmore, G., Clauser, C. & Roy, S., 2016. ISRM suggested methods for determining thermal properties of rocks from laboratory tests at atmospheric pressure, *Rock Mech. Rock Eng.,* **49,** 4179–4207.

Popov, Y.A., Pribnow, D.F.C., Sass, J.H., Williams, C.F. & Burkhardt, H., 1999. Characterization of rock thermal conductivity by high-resolution optical scanning, *Geothermics,* **28,** 253–276.

Pribnow, D. & Umsonst, T., 1993. Estimation of thermal conductivity from the mineral composition: influence of fabric and anisotropy, *Geophys. Res. Lett.,* **20,** 2199–2202.

Pribnow, D.F.C. & Sass, J.H., 1995. Determination of thermal conductivity for deep boreholes, *J. geophys. Res.,* **100,** 9981–9994.

Ray, L., Förster, H.-J., Förster, A., Fuchs, S., Naumann, R. & Appelt, O., 2015. Tracking the thermal properties of the lower continental crust: measured versus calculated thermal conductivity of high-grade metamorphic rocks (Southern Granulite Province, India), *Geothermics,* **55,** 138–149.

Schmitt, D.R., Han, Z., Kravchinsky, V.A. & Escartin, J., 2007. Seismic and magnetic anisotropy of serpentinized ophiolite: implications for oceanic spreading rate dependent anisotropy, *Earth planet. Sci. Lett.,* **261,** 590–601.

Schön, J.H., 2011. Nuclear magnetic resonance—petrophysical properties, in *Handbook of Petroleum Exploration and Production,* Vol. 8, pp. 75–96, Elsevier. https://doi:10.1016/S1567-8032(11)08003-7.

Song, I., Suh, M., Woo, Y.-K. & Hao, T., 2004. Determination of the elastic modulus set of foliated rocks from ultrasonic velocity measurements, *Eng. Geol.,* **72,** 293–308.

Surma, F. & Geraud, Y., 2003. Porosity and thermal conductivity of the Soultz-sous-Forêts granite, *Pure appl. Geophys.,* **160,** 1125–1136.

Vielzeuf, D. & Kornprobst, J., 1984. Crustal splitting and the emplacement of Pyrenean lherzolites and granulites, *Earth planet. Sci. Lett.,* **67,** 87–96.

Vosteen, H.-D. & Schellschmidt, R., 2003. Influence of temperature on thermal conductivity, thermal capacity and thermal diffusivity for different types of rock, *Phys. Chem. Earth Parts ABC,* **28,** 499–509.

Wang, Q., Ji, S., Sun, S. & Marcotte, D., 2009. Correlations between compressional and shear wave velocities and corresponding Poisson's ratios for some common rocks and sulfide ores, *Tectonophysics,* **469,** 61–72.

Xu, Y., Shankland, T.J., Linhardt, S., Rubie, D.C., Langenhorst, F. & Klasinski, K., 2004. Thermal diffusivity and conductivity of olivine, wadsleyite and ringwoodite to 20 GPa and 1373 K, *Phys. Earth planet. Inter.,* **143-144,** 321–336.

Yaşar, E., Erdoğan, Y. & Güneyli, H., 2008. Determination of the thermal conductivity from physico-mechanical properties, *Bull. Eng. Geol. Environ.,* **67,** 219–225.

Yu, R., Jiang, S., Wang, H., Du, F., Zhang, L., Wen, Y., Luo, C. *et al.*, 2022. Estimation of thermal conductivity of plutonic drill cuttings from their mineralogy: a case study for the FORGE Well 58–32, Milford, Utah, *Geothermics,* **102,** 102407.

Zamora, M., Vo-Thanh, D., Bienfait, G. & Poirier, J.P., 1993. An empirical relationship between thermal conductivity and elastic wave velocities in sandstone, *Geophys. Res. Lett.,* **20,** 1679–1682.

Zhang, B., Ge, J., Xiong, Z. & Zhai, S., 2019. Effect of water on the thermal properties of olivine with implications for lunar internal temperature, *J. geophys. Res.,* **124,** 3469–3481.

Zhao, X.G., Wang, J., Chen, F., Li, P.F., Ma, L.K., Xie, J.L. & Liu, Y.M., 2016. Experimental investigations on the thermal conductivity characteristics of Beishan granitic rocks for China's HLW disposal, *Tectonophysics,* **683,** 124–137.

APPENDIX

The individual mean mineral TC, the TC fluid saturating pores (λ_i; Table 2) and the volume fraction (X_i) of the *i*th phase relative to the total volume (considering porosity) were used to calculate the TC (λ_{cal}) using the mixing models (eqs A1–A9):

$$\lambda_{ari} = \sum_{i=1}^{n} (\lambda_i * X_i), \tag{A1}$$

where λ_{ari} is the arithmetic mean model, λ_i is the mean TC of the *i*th mineral phase and fluid suturing pores, and X_i is the volume friction of *i*th mineral phase and porosity.

$$\lambda_{har} = \left[\sum_{i=1}^{n} (X_i/\lambda_i)\right]^{-1}, \tag{A2}$$

where λ_{har} is the harmonic mean model.

$$\lambda_{VRH} = \frac{1}{2}(\lambda_{ari} + \lambda_{har}), \tag{A3}$$

where λ_{VRH} is the Voigt–Reuss–Hill mean mode.

$$\lambda_{geo} = \prod_{i=1}^{n} \lambda_i^{xi}, \tag{A4}$$

where λ_{geo} is the geometric mean model.

$$\sqrt{\lambda_{sqr}} = \sum_{i=1}^{n} \sqrt{x_i \lambda_i}, \tag{A5}$$

where λ_{sqr} is the square roots mean model.

$$\lambda_{HS}^{+} = \lambda_{max} + \frac{A_{max}}{1 - A_{max}\alpha_{max}},$$

where $A_{max} = \sum_{i=1;\ \lambda_i \neq \lambda_{max}}^{n} \left(\frac{x_i}{\alpha_{max} + 1/(\lambda_i - \lambda_{max})}\right)$, $\lambda_{max} = \max(\lambda_1 \ldots \lambda_n)$, $\alpha_{max} = \frac{1}{3\lambda_{max}}$, and $\lambda_{HS}{}^{+}$ is the upper bound of Hashin–Shtrikman mean model,

$$\lambda_{HS}^{-} = \lambda_{min} + \frac{A_{min}}{1 - A_{min}\alpha_{min}}, \tag{A6}$$

where $A_{min} = \sum_{i\ =\ 1;\ \lambda_i \neq \lambda_{min}}^{n} \left(\frac{x_i}{\alpha_{min} + 1/(\lambda_i - \lambda_{min}}\right)$, $\lambda_{min} = \min(\lambda_1 \ldots \lambda_n)$, $\alpha_{min} = \frac{1}{3\lambda_{min}}$ and $\lambda_{HS}{}^{-}$ is the lower bound of Hashin–Shtrikman mean model,

$$\lambda_{HS} = \frac{1}{2}(\lambda_{SH}^{l} + \lambda_{SH}^{u}) \tag{A7}$$

where λ_{HS} is the Hashin–Shtrikman mean model.

$$\lambda_{eff} = 1/\left(\sum_{i=1}^{n} \frac{3x_i}{(2\lambda_{VRH} + \lambda_i)}\right) \tag{A8}$$

where λ_{eff} is the effective mean model.

$$\lambda_{QPS} = \frac{1}{2}(\lambda_{sqr} + \lambda_s) \tag{A9}$$

where $(\lambda_s)^{-1/2} = \sum_{i\ =\ 1}^{n} X_i(\lambda_i)^{-1/2}$, λ_{QPS} is the Robertson and Pack model.